Advancing CLMU for regional urban climate simulations through WRF coupling: intercomparison with NOAH–SLUCM

Yuan Sun¹, Keith W. Oleson², Cenlin He³, Zhonghua Zheng¹

- ¹Department of Earth and Environmental Sciences, The University of Manchester, Manchester M13 9PL,
 - ²Climate and Global Dynamics Laboratory, NSF National Center for Atmospheric Research, Boulder, CO 80307, USA
 - ³Research Applications Laboratory, NSF National Center for Atmospheric Research, Boulder, CO 80307, USA

Key Points:

10

12

13

15

- We apply WRF-CLMU for high-resolution (1.2 km) regional urban climate simulations over Greater Manchester, compared with WRF-SLUCM.
- Both models simulate monthly mean near-surface air temperature, humidity, and wind speed comparably against three observation stations.
- WRF-CLMU reproduces extreme land surface temperatures consistent with remote sensing during the 2022 July heatwave.

Corresponding author: Yuan Sun, yuan.sun@manchester.ac.uk

Corresponding author: Zhonghua Zheng, zhonghua.zheng@manchester.ac.uk

Abstract

Urban areas are highly vulnerable to climate extremes, creating a pressing need for reliable modeling tools to support climate adaptation. The Weather Research and Forecasting (WRF) model is widely used for regional urban climate simulations, and incorporating an alternative urban scheme for long-term climate projections expands the available modeling options and supports more robust simulation outcomes. This study evaluates the performance of Community Land Model-Urban (CLMU) via WRF coupling (WRF-CLMU), in comparison with the default WRF single-layer urban canopy model (WRF-SLUCM). We take Greater Manchester, UK, as a testbed under a grid spacing of 1.2 km for the year 2022. Model performance is assessed using near-surface air temperature, relative humidity, and wind speed from three observational stations, along with land surface temperature (LST) from MODIS and VIIRS 1 km products. The results demonstrate that both models have comparable performance, while WRF-CLMU better captures extreme heat conditions on 16 July, the onset of the 2022 July heatwave, as indicated by 1-2°C higher daytime LSTs in the main urban area. On the first day of the heatwave, it simulates daytime surface urban heat island intensity of 9.0°C, in agreement with the satellite-based estimates from MODIS (9.0°C) and VIIRS (10.0°C). These findings improve our understanding of WRF-CLMU behavior and highlight its potential applications for future high-resolution regional urban climate simulations.

Plain Language Summary

Cities are especially vulnerable to extreme weather, and reliable computer models are needed to help plan for climate change. The Weather Research and Forecasting (WRF) model is widely used to study weather and climate in urban areas, and its performance can vary depending on the urban scheme used. In this study, we evaluate the performance of the Community Land Model-Urban (CLMU) when coupled with WRF for regional urban climate simulations. We conduct simulations at 1.2 km spatial resolution over Greater Manchester, UK, and compare WRF-CLMU results with WRF's default urban scheme, NOAH-SLUCM. Both models reproduce the observed monthly average near-surface air temperature, humidity, and wind speed reasonably well. On the onset of the 2022 July heatwave, WRF-CLMU simulates 1–2°C higher land surface temperatures than WRF-SLUCM in the main urban area, thereby better capturing the extreme heat conditions. These results highlight the potential of WRF-CLMU for future applications in high-resolution urban climate modeling and climate impact assessments.

1 Introduction

Mesoscale urban climate modeling spans from individual cities to larger urban and surrounding regions, typically using horizontal length scales of approximately 25 km and 100 km, respectively (Oke et al., 2017). Such scales require a balance between model complexity (e.g., physics, spatial resolution) and computational efficiency. As a mesoscale numerical weather prediction system, the Weather Research and Forecasting (WRF) model has been widely used in urban weather and climate studies (e.g., Georgescu et al., 2024; Krayenhoff et al., 2018; Khan et al., 2024; Qian et al., 2022; Salamanca et al., 2018; Zhao et al., 2021). WRF offers three urban models with varying levels of complexity (Chen et al., 2011; Joshi et al., 2025): the single-layer urban canopy model (SLUCM) (Kusaka et al., 2001; Kusaka & Kimura, 2004), the building effect parameterization (BEP) (Martilli et al., 2002), and the BEP with building energy model (BEP/BEM) (Salamanca & Martilli, 2010). Each of these schemes is implemented separately and can be run independently within WRF. They are integrated within the generic Noah family of land surface models (LSMs), including Noah LSM and NoahMP LSM. Hereafter, we refer to them collectively as NOAH-LSM.

68

71

72

73

74

75

76

79

80

81

82

83

87

88

89

91

95

96

97

100

101

102

103

104

106

107

108

109

110

111

112

114

115

116

117

118

119

120

Besides NOAH-LSM, WRF also provides another land surface scheme derived from the Community Land Model version 4 (CLM4) (Oleson, Lawrence, et al., 2010; Xu et al., 2020). CLM is the land component of the Community Earth System Model (CESM), which features an explicit representation of land surface processes among vegetation, snow, soil, and so on (Danabasoglu et al., 2020). It includes an urban component, known as the Community Land Model-Urban (CLMU). Over the past decades, CLMU has evolved in parallel with CLM, progressing through versions such as CLMU4 (Oleson, Bonan, et al., 2010), CLMU4.5 (Oleson et al., 2013), and CLMU5 (Oleson & Feddema, 2020). Compared with earlier versions, CLMU5 includes updated urban thermal and radiative parameter datasets and an explicit building energy model. Post-CLMU5 versions introduce additional functionalities, such as an explicit air-conditioning parameterization (X. C. Li et al., 2024) and transient urban land cover representation (K. Zhang et al., 2025). Alongside its continued development, CLMU enables global urban climate simulations (e.g., Y. Sun et al., 2024; Zhao et al., 2021; Zheng et al., 2021) within an Earth system modeling framework, as well as regional (e.g., C. Li et al., 2023; L. Wang et al., 2025) and single-point (e.g., Y. Sun, Oleson, Zhao, et al., 2025; Y. Sun, Oleson, & Zheng, 2025; Yu et al., 2025) applications. Previous studies have also comparatively evaluated CLMU and other urban models through regional climate simulations (e.g., Imran et al., 2018; Karlický et al., 2018; Zhao et al., 2021). However, after CLMU4 was embedded within a simplified version of CLM4 as the land surface scheme in WRF, the development of CLM and WRF has since diverged, and CLMU5 has not yet been coupled with any regional atmospheric models. Consequently, regional urban climate studies (e.g., C. Li et al., 2023; L. Wang et al., 2025) have to rely on offline CLMU5 simulations that exclude atmosphereland interactions. For example, C. Li et al. (2023) resampled atmospheric forcing data from 0.1° to drive CLMU5 with a grid spacing of 1 km over Nanjing, China, while L. Wang et al. (2025) conducted 0.125° simulations in CLMU5 with 12 km atmospheric forcings over the contiguous US. In such setups, urban processes are limited by the absence of atmospheric feedback and the coarse spatial-temporal resolution of prescribed atmospheric forcing data (Tsiringakis et al., 2019). Moreover, evaluations of CLMU5 to date have also been limited to land-only/offline mode (e.g., Lipson et al., 2023; Zhao et al., 2021).

Recently, the Community Terrestrial Systems Model (CTSM), the successor to CLM5, has been coupled to WRF via the Lightweight Infrastructure for Land-Atmosphere Coupling (LILAC) framework, beginning with CTSM version tag CTSM1.0.dev104 (CTSM Development Team, 2024; Huang et al., 2025; Mužić et al., 2025). Unlike earlier approaches that directly embedded CLM4 with WRF, LILAC serves as an external coupler that links WRF and CTSM while maintaining the structural integrity of both models. As a result, LILAC provides greater flexibility, facilitates customized model configurations, and enables easier model version updates. Mužić et al. (2025) performed the first WRF-CTSM experiment over Northern Europe using a single domain at 10.5 km resolution to evaluate hydroclimatic variables. Although the coupling approach was not originally designed for urban climate modeling, it provides several potential benefits for regional urban climate studies (Figure 1). First, in terms of application, it extends CLMU's capability at the meso/kilometer scale with two-way atmosphere-land interactions. Since CLMU is specifically designed for long-term climate projections rather than short-term weather prediction, this online modeling framework enables the application of CLMU's recent developments to specific urban regions. Second, regarding model configuration and user flexibility, it alleviates limitations imposed by the availability and quality of atmospheric forcing data to drive CLMU, allowing users to define spatial resolutions and simulation periods according to their needs. Third, from a community perspective, linking CLMU with WRF allows its inclusion in multi-model intercomparison efforts alongside urban climate schemes such as WRF-SLUCM, WRF-BEP, WRF-BEP/BEM, WRF-ASLUM (C. Wang et al., 2021), WRF-SUEWS (T. Sun et al., 2024), WRF-TEB (Meyer et al., 2020), WRF-VUCM (Lee et al., 2016), and WRF-ELM-Urban (Huang et al., 2025), thereby supporting ensemble-based regional urban climate simulations. However, the single-domain WRF-CTSM configuration described by Mužić et al. (2025) is not directly applicable to

regional urban climate simulations, which require high-resolution grid spacing and explicit urban canopy representation.

122

123

124

125

126

127

128

130

131

132

133

134

135

136

137

138

139

140

141

143

144

145

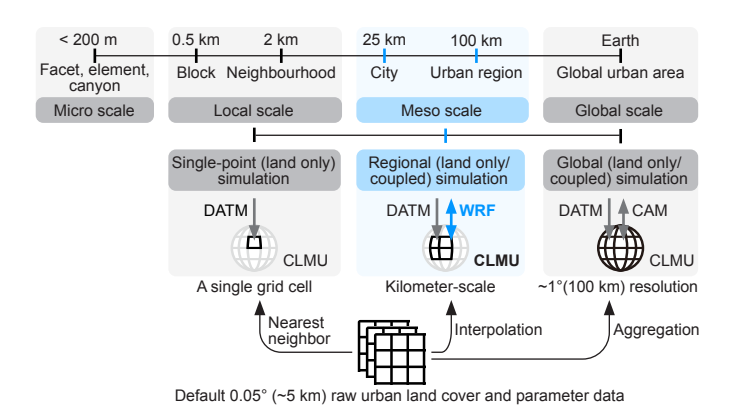


Figure 1. Capability of the Community Land Model-Urban (CLMU) in multi-scale urban climate modeling. CLMU is a single-layer urban canopy model, making it suitable for local, meso-, and global-scale simulations. Note that CLMU is unsuitable for micro-scale simulations where explicit horizontal variability needs to be resolved. The default raw urban land cover and parameter data for generating CLMU surface inputs are provided at a spatial resolution of 0.05° (~5 km), with different algorithms (e.g., nearest neighbor, interpolation, aggregation) to customize the simulation grid spacing. DATM is atmospheric forcing data, supported by the Community Data Models for Earth Predictive Systems (CDEPS). WRF is the Weather Research and Forecasting Model. CAM is the Community Atmosphere Model. Classification of the typical horizontal length scales, urban units, and climate scales follows Oke et al. (2017).

As a first step toward advancing the application of WRF-CTSM in mesoscale urban climate research, this study develops an urban-focused WRF-CLMU workflow and evaluates its performance against WRF-SLUCM and observational data. The Greater Manchester area in the UK is used as a testbed, with a grid spacing of 1.2 km. Both CLMU and NOAH-SLUCM are based on single-layer urban canopy representations, where the near-surface canopy air mediates the exchange of energy and water between the atmosphere and the land surface (Masson et al., 2008). While the International Urban Energy Balance Models Comparison Project (PILPS-Urban) (Grimmond et al., 2010, 2011) and Urban-PLUMBER project (Lipson et al., 2022, 2023) has primarily assessed both models using single-point offline simulations, the present study conducts a comparative evaluation within a coupled atmosphere-land configuration, incorporating each land surface model's respective representation and physical parameterization schemes. This approach enables the evaluation of the representation of urban regions and the spatial distribution of climate variables (i.e., urban, suburban, rural). The objective is to highlight similarities and differences in model complexity and configuration, as well as interpret variations in the simulated results and their underlying physical causes.

This paper is structured as follows: Section 2 describes the methodology of intercomparisons between CLMU and NOAH-SLUCM, including a literature review and their applications via WRF coupling over Greater Manchester. Section 3 evaluates the models against observations and discusses the model sensitivity by perturbing urban parameters. Finally, Section 4 summarizes the key findings and outlines future directions for advancing WRF-CLMU.

2 Method and Data

2.1 Intercomparisons between CLMU and NOAH-SLUCM

Both NOAH-SLUCM and CLMU represent urban surfaces using a simplified urban canyon approach, yet they are fundamentally distinct models. Table 1 summarizes the main features of the two models with both default and detailed configuration options. Generally, NOAH-SLUCM is designed for numerical weather prediction and short-term forecasting (e.g., from days to seasons) as a schematic option within WRF. As a regional climate model, WRF couples the atmosphere and land components. By contrast, CLMU is developed for climate modeling and long-term projection (e.g., from years to decades) as the default urban scheme in CESM (and its land component, CTSM), an Earth system model that integrates multiple Earth components.

Table 1. Lists of Urban Representations and Parameterizations in NOAH-SLUCM and CLMU.

Objective Setting		NOAH Single Layer Urban Canopy Model (NOAH-SLUCM)	Community Land Model-Urban (CLMU)		
Primary use	Default	For numerical weather prediction and short-term forecasting	For climate modeling and long-term projection		
Land model com- plexity	Default	More simplified non-urban treatments in NOAH-LSM but computationally faster	More detailed non-urban representation in CLM but computationally heavier		
	Detailed	Not applicable	A fast structure as simplification (Table B2)		
Land data	Default	MODIS IGBP 21-category data	Land Use Harmonized version 2 (LUH2) transient land use and land cover change dataset (Lawrence et al., 2019)		
Urban land cover	Default	Static	Static		
representation	Detailed	None	Transient (annual, 2000-2100) (Gao & O'Neill, 2020; K. Zhang et al., 2025)		
Urban types per grid cell	Default	One urban class: urban and built-up	Three urban classes: tall building district (TBD), high-density (HD), and medium-density (MD) (Jackson et al., 2010)		
	Detailed	Eleven urban classes: local climate zones (LCZs) (Demuzere et al., 2022, 2023); three urban classes: commercial, high intensity residential, low intensity residential (D. Li et al., 2013)	One urban class: TBD or HD or MD; ten urban classes: LCZs* (Y. Sun, Oleson, Zhao, et al., 2025)		
Terminology of urban land cover	Default	Urban fraction (FRC_URB) is defined as the proportion of impervious surfaces (i.e., buildings, roads, walls) within the portion of a grid cell that is designated as urbanized land.	Percentage of urban area (PCT_URBAN) is defined as the proportion of the total land area of a grid cell that is classified as urban land-units mixing urban impervious and pervious fractions.		
Urban facades	Default	Three types: roof, wall, and road	Five types: roof, sunlit wall, shaded wall, pervious floor, and impervious floor		
Urban parameters	Default	A look-up table of parameters based on urban classes without spatial variability	2-dimensional distributed map (interpolated from 0.05° raw data, with variability specified across 33 global regions) (Jackson et al., 2010)		
	Detailed	1 km 2-dimensional distributed map* (Liao et al., 2025)	1 km 2-dimensional distributed map* (Cheng et al., 2025)		
Urban thermal properties	Default	$4\ \mathrm{layers}$ for roof, wall, and road; each having the same thermal properties	10 layers for roof and wall, 2–3 layers for impervious floor; thermal properties varying by layer to reflect depth-dependent material properties		
	Detailed	None	User-defined number of layers for roof, wall, and impervious floor		
Urban vegetation	Default	Lacking a specific scheme, instead deriving energy and water fluxes from natural vegetation and soil processes externally modeled by NOAH-LSM	A simplified bulk soil scheme that parametrizes pervious floor as bulk soil for energy and water exchange		
Anthropogenic heat flux	Default	Disabled	Sensible heat flux from building space heating and air conditioning (Oleson & Feddema, 2020)		
	Detailed	Prescribed as constant or time-varying sensible and latent heat fluxes (Varquez et al., 2021); online building energy modeling* (Takane et al., 2024)	Explicit air-conditioning adoption (X. C. Li et al., 2024); online traffic heat modeling* (Y. Sun, Oleson, & Zheng, 2025)		
Building ventila- tion heat	Default	None	Quantified based on outdoor-indoor temperature gradient (Oleson & Feddema, 2020)		
Radiation scheme	Default	Single reflection (Joshi et al., 2025)	Multiple reflection within the urban canyon (Oleson, Bonan, et al., 2010)		
Turbulent heat transfer	Default	Roof \rightarrow atmosphere; wall/road \rightarrow canopy air	Roof/sunlit wall/shaded wall/pervious floor/impervious floor \rightarrow canopy air \rightarrow atmosphere		
2m air tempera- ture	Default	Diagnostic, estimated from stability-corrected empirical coefficients (Kanda et al., 2007)	Alternatively represented by the canopy air temperature in an iterative approach		
Additional func- tionalities	Detailed	Green roof irrigation (Yang et al., 2015), etc.	Green roof irrigation* (L. Wang et al., 2021); transient urban albedo* (Y. Sun et al., 2024), etc.		

- 1 This table is based on WRF v4.7.0 (https://github.com/wrf-model/WRF/tree/release-v4.7.0, last access: 26 November 2025), and CTSM 5.3.024 (https://github.com/ESCOMP/CTSM/tree/ctsm5.3.024, last access: 26 November 2025) (CTSM Development Team, 2025). Some of the "detailed" functionalities tagged with asterisk (*) are recent developments that may not yet be fully integrated into the community version of WRF or CTSM.
- 2 Representing a single urban land cover class per grid cell is referred to as the "dominant" approach, whereas representing multiple urban classes within a grid cell is known as the "mosaic" approach, allowing subgrid-level resolution of urban land-units.
- 3 Within the CTSM's fast model configuration, collapse_urban = .true. is enabled by default (Table B2). This setting reduces computational cost by representing only one urban class per grid cell during the model initialization. The areal fractions of all urban classes are summed to give the total percentage of urban areas, while the physical parameter values are assigned from the urban class with the largest areal fraction.

158

159

161

162

163

165

166

168

169

170

171

172

173

174

175

177

178

These two urban models differ in how they interface with their respective land surface models. NOAH-SLUCM assigns each grid cell a dominant land cover type, with urban and built-up as a single category. For grid cells classified as urban, the model does not treat them as fully urbanized; instead, it partitions the grid cell into an urban impervioussurface fraction (FRC_URB) and an urban pervious-surface fraction (1-FRC_URB), considering urban vegetation (Figure 2(a)). This representation differs from both a fully dominant scheme and a true mosaic approach: only two fractions are represented, yet the cell is still classified as urban at the grid level. Here, we follow D. Li et al. (2013) in referring to this as a "dominant" urban land cover approach, since only one urban land cover type is available. Note that the "dominant" designation only determines whether a grid cell is classified as urban; it does not constrain the values of FRC_URB and 1-FRC_URB, which can be specified or adjusted by users. Comparatively, CLMU's overlying CTSM adopts a "mosaic" approach to work for coarse-resolution Earth system modeling, in which each grid cell is subdivided into subgrid land-units (i.e., natural vegetation, crop, lake, glacier, urban classes) and further into sub-subgrid columns (e.g., roof, wall) (Figure 2(b)). Urban land-units are categorized into three types at the subgrid level: tall building district (TBD), high-density (HD), and medium-density (MD), each contributing to the overall grid-cell via area fractions. While atmospheric forcing is applied uniformly across the grid cell, feedback to the atmosphere is aggregated from all subgrid land-units through area-weighting. This area-weighted aggregation is similarly done for NOAH-SLUCM, which also represents urban and non-urban processes to compute grid-cell fluxes to the atmosphere.

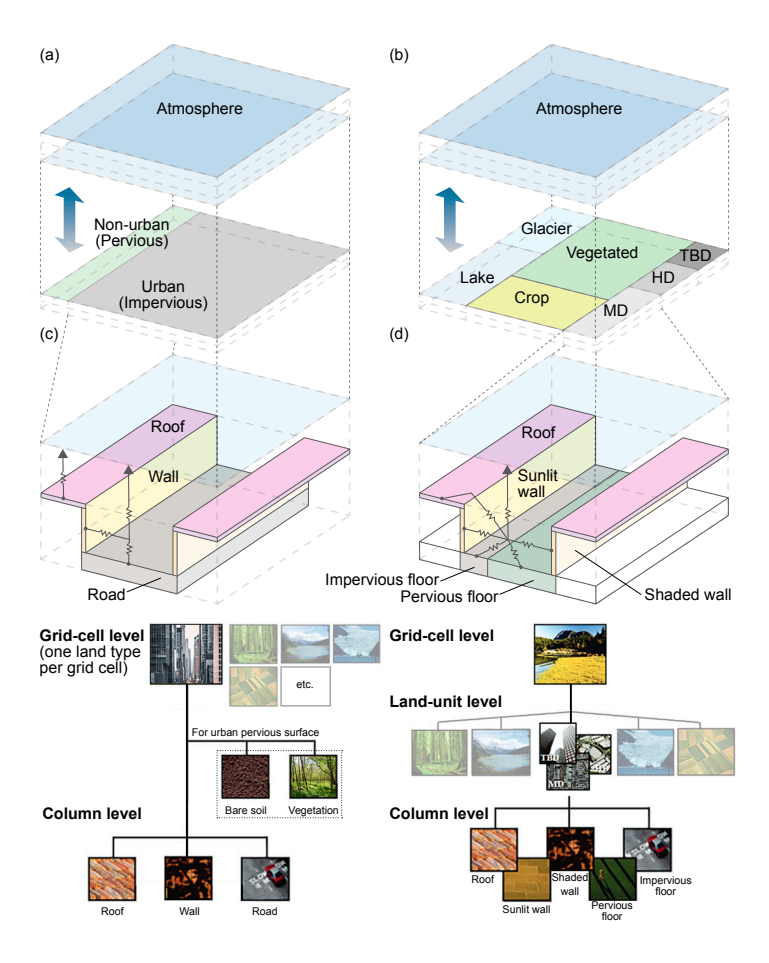


Figure 2. Urban representation in land surface models. (a) A grid cell in the NOAH land surface model (NOAH-LSM) using a "dominant" approach to representing urban. The urban fraction refers to urban impervious surfaces; the non-urban fraction represents pervious surfaces, which are modeled separately from the urban model. (b) A grid cell in the Community Terrestrial Systems Model (CTSM) using a "mosaic" approach to representing the land surface. Urban land cover is classified as tall building district (TBD), high-density (HD), and medium-density (MD). (c) Urban surface representation in the NOAH single-layer urban canopy model (NOAH-SLUCM). (d) Urban surface representation in the Community Land Model-Urban (CLMU). Both land surface models interact with the atmospheric model at the grid level, aggregating subgrid fluxes through areal weighting. In grid cells dominated by urban areas, NOAH-LSM derives energy and water fluxes for the urban pervious-surface portion based on natural vegetation and soil.

The two models adopt different parameterization schemes for urban physics. Compared to NOAH-SLUCM, CLMU provides more explicit parameterizations of energy and water exchanges among urban canopy air, surfaces, and building interiors. For example, NOAH-SLUCM includes three facades: roof, the wall, and road, parameterized by empirical schemes based on observational constraints (Figure 2(c)). Wall and canyon floor interact with the urban canopy layer, whereas the roof directly responds to the lowest atmospheric layer. By contrast, CLMU uses more physically based formulations, allowing it to separately resolve sunlit and shaded walls, and differentiate between impervious and pervious canyon floors by explicitly solving surface energy balance (Figure 2(d)). CLMU places greater importance on the urban canopy air as a mediator for interactions among all surfaces, the canopy layer, and the overlying atmosphere. This method is de-

rived from the Town Energy Balance (TEB) model (Masson, 2000). As suggested by Barbano et al. (2021), rooftop-level fluxes are primarily governed by the canopy layer rather than being directly coupled to the free atmosphere. In efforts to connect the roof to the atmosphere for CLMU, the roof surface cools down through atmospheric exchange, reducing the mean bias error (MBE) for summer roof surface temperature from 5.9° C to 3.6° C (Demuzere et al., 2013). Moreover, NOAH-SLUCM excludes urban vegetation from its urban canopy modules but simulates energy and water exchanges for the vegetated and soil portions using the standard NOAH-LSM. By contrast, CLMU represents urban vegetation as pervious surfaces on the canyon floor and parameterizes them similarly to a bulk soil layer within the urban module itself. Regarding anthropogenic heat flux, NOAH-SLUCM assigns a default of 0 W/m² (tunable based on applications and observations), whereas CLMU incorporates a building energy model by default to estimate anthropogenic heat flux based on more explicit space heating and air conditioning (Oleson & Feddema, 2020).

In terms of usability, NOAH-SLUCM offers a relatively simple default configuration, with several advanced options that can be activated based on applications, such as green roof irrigation (Yang et al., 2015), time-varying prescribed anthropogenic heat flux (Varquez et al., 2021), and 2-dimensional distributed urban parameter maps (Liao et al., 2025). The model remains highly flexible and highly customizable, allowing users to tailor it to a wide range of regional urban study needs. Conversely, CLMU, being developed within the Earth system model framework of CESM, is more tightly integrated and less user-friendly for customizing urban configurations. Because CESM is originally designed for global simulations, using CLMU for local-scale urban climate applications requires additional high-resolution input data (e.g., Cheng et al., 2025) or more detailed land cover classification (e.g., Y. Sun, Oleson, Zhao, et al., 2025) to accurately capture urban land cover heterogeneity.

2.2 Schematic of Workflow Development

We develop an urban-focused workflow of coupling WRF and CLMU to enable high-resolution urban climate simulations. This workflow follows the guides of University Corporation for Atmospheric Research (UCAR) (2020) and adapts scripts from CTSM-Norway (2024), which provides instructions for converting WRF-defined domains into CTSM5.1-compatible surface and mesh data. Building on these advances, our workflow is designed for high-resolution, nested-domain WRF-CTSM applications supported by the Earth System Modeling Framework (ESMF) (ESMF Core Team, 2025). Unlike the single-domain WRF-CTSM simulations at relatively large scales, as described by CTSM-Norway (2024), applying WRF-CLMU to urban studies requires the use of nested domains as part of a dynamical downscaling process. This is a one-way nesting (outer-to-inner domain) approach to capturing urban climate signals. The whole workflow includes three steps (Figure 3): (1) generate static surface data for all domains; (2) perform a WRF-only nested simulation for the outer domains; and (3) conduct WRF-CTSM simulations for the innermost domain.

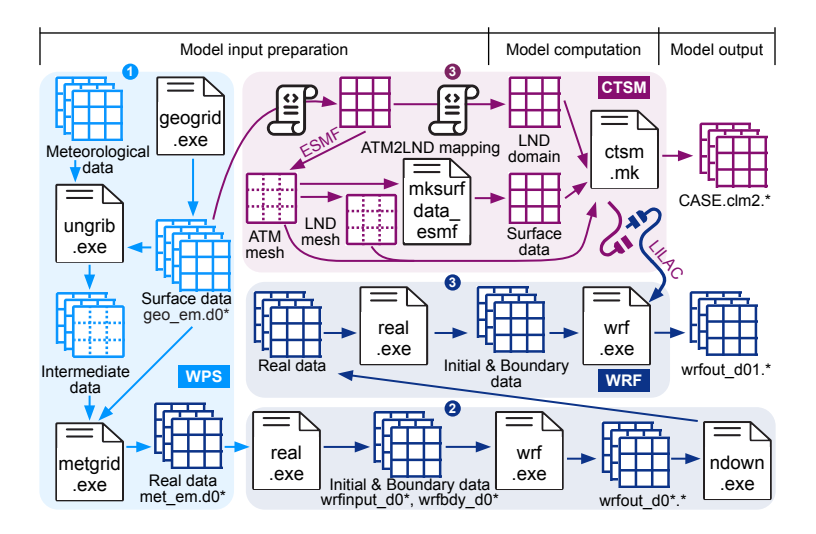


Figure 3. General workflow of coupling the Weather Research and Forecasting model (WRF) and Community Terrestrial Systems Model (CTSM). The Lightweight Infrastructure for Land-Atmosphere Coupling (LILAC) serves as CTSM's interface with WRF. Both CTSM and LILAC rely on functions provided by the Earth System Modeling Framework (ESMF) (ESMF Core Team, 2025).

Unlike NOAH-LSM, which is tightly integrated into WRF and automatically built into its compiled executable, wrf.exe, configuring WRF-CLMU is relatively complicated. Specifically, at the model installation stage, users need to build an additional ctsm.mk makefile fragment and then use it during the WRF compilation process. For certain simulations, the WRF Preprocessing System (WPS) provides static geographic inputs for target domains, which can be directly used by WRF-SLUCM. By contrast, these WPS outputs are not directly compatible with CTSM, which requires land surface data generated via its mksurfdata_esmf tool. To ensure consistency in spatial resolution between the atmosphere and the land component, land mesh and domain data are mapped from the WPS outputs and used for indexing land grid cells. Compared with earlier CLM5 versions, CTSM now uses updated annual urban land cover datasets, providing year-specific urban 3-class fractions (https://svn-ccsm-inputdata.cgd.ucar.edu/trunk/inputdata/lnd/clm2/rawdata/gao_oneill_urban/, last access: 26 November 2025) (Gao & O'Neill, 2020).

Due to its detailed physical processes and land surface representation, WRF-CLMU is computationally expensive. Even under CTSM fast model configuration, WRF-CLMU requires about 1–2 times more computing resources than WRF alone (Table B2, Figure B1). Consequently, the simulation time step should consider both grid spacing constraints and CTSM computation, as the land component can be slower than the atmospheric component. Under such intensive computational loads, CPU performance can also become a limiting factor. Despite these additional costs, WRF-CLMU enables more process-level analyses of the urban climate system. In addition to standard WRF outputs, CTSM can provide fields along its representation hierarchy, including the grid level, subgrid/land-unit level (i.e., TBD, HD, MD), and sub-subgrid/column level (i.e., roof, wall, sunlit wall, shaded wall, pervious floor, impervious floor), depending on user-specified name-list settings.

2.3 Study Area: Greater Manchester

257

258

259

260

261

262

263

266

268

269

273

274

275

Greater Manchester (GM), located in the North West of England, historically experienced a temperate climate. It has recently faced increasing heat risk, as exemplified by heatwave events in 2022, when the heatwave from 16 to 19 July was record-breaking. We use the WRF4.7.0 and CTSM5.3.024 in a coupled mode. GM_SLUCM and GM_CLMU refer to two simulations: coupling WRF with NOAH-SLUCM, and WRF with CLMU, respectively (Table 2). Both simulations are initialized on 25 December 2021, allowing for a one-week spin-up before analyzing the full year of 2022. In regional simulations, a short atmospheric spin-up is often sufficient due to the strong constraint from large-scale forcing.

Table 2. Summary of Simulation Cases.

Objective	Model and do- main	Simulation name	Simulation period	Period for analysis	Atmospheric initialization	Land initializa- tion	Urban parameter setting
Dynamical downscal- ing	WRF with d01, d02, and d03	_	25 December 2021 to 31 December 2022	-	Cold start	Initial data generated by WPS	Using WRF default urban parameter look-up table
Model eval- uation	WRF with d04	GM_SLUCM	25 December 2021 to 31 December 2022	1 January 2022 to 31 December 2022	Cold start	Initial data gener- ated by WPS	Using WRF default urban parameter look-up table
	WRF- CTSM with d04	GM_CLMU	25 December 2021 to 31 December 2022	1 January 2022 to 31 December 2022	Cold start	Initial data inter- polated by CTSM	Using CESM default 2- dimensional urban parameters
Model sen- sitivity	WRF-CTSM with d04	$\begin{array}{c} {\rm GM_CLMU_{ALB}} \\ {\rm GM_CLMU_{ALB}} \end{array}$	16–19 July 2022 25 December 2021 to 6 January 2022	16–19 July 2022 4–6 January 2022	Use restart data from GM_CLMU Cold start	Use restart data from GM_CLMU Initial data inter- polated by CTSM	Changing albedo of impervious floor and pervious floor to 0.23
			25 December 2021 to 6 January 2022 11–19 July 2022	4–6 January 2022 16–19 July 2022	Cold start Use restart data from GM_CLMU	Initial data inter- polated by CTSM Initial data inter- polated by CTSM	Changing morphological, radiative, and thermal parameters the same as GM_SLUCM

- 1 Model-specific urban parameters are listed in Table B1.
- 2 To accelerate WRF-CLMU simulations, we adopt the majority of name-list settings for the fast configuration (Table B2), except that we disable n_dom_landunits = .true. to avoid overly simplifying the urban representation when the percentage of urban area is small.
- 3 GM_CLMU_{NOAH} disables the quantification of building spacing heating, or air conditioning, whereas GM_CLMU and GM_CLMU_{ALB} retain these processes by default. GM_SLUCM sets anthropogenic heat as $0~\rm W/m^2$ by default.
- 4 If the atmospheric model is initialized with a cold start, early simulation periods are reserved for model spin-up and omitted from the analysis.

Before running the GM_SLUCM and GM_CLMU simulations, we conduct a three-domain (i.e., d01, d02, d03) nested WRF simulation to progressively downscale ERA5 reanalysis at a spatial resolution of 0.25° (~25 km) to a refined resolution of 3.6 km. This simulation followed the same configurations as described in Table 3, with additionally upper-air analysis nudging applied every 6 hours. The output from the third domain (d03) then serves as the initial and boundary conditions for the fourth, innermost domain (d04) at 1.2 km for the GM_SLUCM and GM_CLMU simulations (Figure 4(a)). This stepwise approach mitigates potential abnormalities caused by directly interpolating ERA5 data from 0.25° to 1.2 km.

Figure 4. Case study area. (a) Domains. (b) Percentage of urban area (PCT_URBAN) for the GM_SLUCM simulation (1.2 km). (c) PCT_URBAN for the GM_CLMU simulation (1.2 km). (d) and (e) are similar to (b) and (d) but showing the fraction of urban impervious surfaces (i.e., roof, wall, road), referred to as the urban fraction (FRC_URB) × 100% in WRF. White lines denote divisions of local authorities in Greater Manchester.

The simulation domains for GM_SLUCM and GM_CLMU are identical in spatial extent, boundary, initial conditions, and atmospheric configuration (Table 3). The only input difference lies in the initialization condition and surface inputs. For land model initialization, NOAH-SLUCM used static data generated by the WPS tool. CLMU generally requires a much longer spin-up to equilibrate variables such as soil moisture and temperature (Jerez et al., 2020). Although it would be normally beneficial to start at a carefully spun-up land state, the computational cost of generating such initial conditions is deemed prohibitive for this study. Therefore, we initialize CLMU using the pregenerated initialization data available in the CTSM input data repository (https://svn-ccsm-inputdata.cgd.ucar.edu/trunk/inputdata/lnd/clm2/initdata_esmf/, last access: 26 November 2025) instead of conducting additional spin-up simulations.

276

277

278

279

280

284

285

Table 3. Configuration for the WRF Atmosphere Component.

Objective	Setting	References
Number of vertical layers	44	_
Grid spacing	1.2 km	_
Initial and boundary conditions	Dynamically downscale from ERA5 reanalysis (Grid spacing: 0.25°)	Hersbach et al. (2023)
Map projection	Lambert conformal conic projection	-
Shortwave and longwave radiation scheme	Rapid Radiative Transfer Model for Global Climate Models (RRTMG) (ra_lw_physics = 4, ra_sw_physics = 4)	Iacono et al. (2008)
Cumulus convection scheme	Disabled (cu_physics = 0)	_
Microphysics scheme	WRF Single-moment 6-class (WSM6) (mp_physics = 6)	Hong and Lim (2006)
Planetary boundary layer scheme	Yonsei University (YSU) scheme with top-down mixing driven by radiative cooling enabled (bl_pbl_physics = 1)	Hong et al. (2006); Wilson and Fovell (2018)
Surface layer scheme	Revised MM5 (sf_sfclay_physics = 1)	Fairall et al. (2003)

1 Convection parameterization is disabled as 1.2 km is convection-permitting scale.

For land surface input, we adopt the default input datasets and schematic settings for both models without further customization, such as implementing LCZ classification or local urban parameters. While the default or out-of-the-box configuration may not reflect the most recent urban developments and local conditions, this model-specific setting serves as a baseline reference for evaluating model behavior. GM_SLUCM represented urban land cover derived from the default 30-second (~1 km) MODIS land cover data representing the year 2004 (Figure 4(b)). The simulation extent has 529.91 km² urban area in total. Urban grid cells with FRC_URB of 0.9 in Greater Manchester suggested that 90% of the urban area is impervious (Figure 4(d)). By contrast, GM_CLMU uses urban land cover data extracted from 0.05° raw data representing the year of 2022, which are interpolated to the 1.2 km grids by the mksurfdata_esmf tool (Figure 4(c)). The total urban area reaches 549.79 km², but only 55% is represented as impervious floor (Figure 4(e)).

To accelerate GM_CLMU simulation, we set the n_dominant_pft = 1 and collapse_urban = .true. in the CTSM configuration, which simplifies the land surface grid cells by a single plant functional type (PFT) (Lombardozzi et al., 2023), and a dominant urban class without changing their areal weights. Given that TBD, MD, and HD urban types contribute to 0%, 2.3%, and 97.7% of urban area across Greater Manchester, collapsing urban types has little effect on the overall urban representation, where the HD fraction ranges from 0% to 11.4% in the main urban area. These differences in land surface input data, along with structural differences in the parameterization schemes of the two land surface models, influence both urban and non-urban processes in the mesoscale simulations and result in varying feedback to the atmosphere.

In addition, we conduct two sensitivity experiments for WRF-CLMU by perturbing urban parameters (Table 2). In the GM_CLMU_{ALB} simulations, the albedo values for both impervious floor (0.13) and pervious floor (0.08) are increased to 0.23, ensuring similar albedo values as in GM_SLUCM, while all other urban parameters remained consistent with the GM_CLMU simulation. In the GM_CLMU_{NOAH} simulation, urban land cover, morphological, radiative, and thermal parameters are set to match those used in the GM_SLUCM simulation. To match the FRC_URB value of 0.9 in GM_SLUCM, we specify 90% PCT_URBAN and 0% urban impervious floor cover in GM_CLMU_NOAH. The remaining 10% of the grid cell land fraction is allocated equally to 5% cropland and 5%

natural vegetation. Building space heating and air conditioning are turned off in GM_CLMU_{NOAH} as well. Instead of depth-dependent material properties, GM_CLMU_{NOAH} adopts single average values of thermal parameters without varying by construction layers, similar to GM_SLUCM .

It is noteworthy that the grid-level outputs from the simulations include contributions from both urban and non-urban fractions. Given that two models differ in their representations, physics, and initial conditions, the sensitivity experiment involving perturbations to urban parameters cannot fully isolate the influence of a single factor (Figure 5). As the primary objective here is to demonstrate the capability of WRF-CLMU, point-to-point control experiments are left for future work.

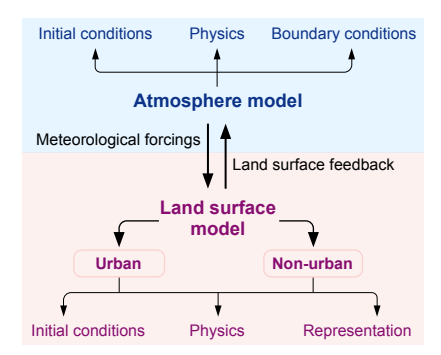


Figure 5. Illustration of factors contributing to simulation differences. The intercomparison of grid-level variables between WRF-SLUCM and WRF-CLMU can be regarded as a comparison between WRF-LSM and WRF-CTSM, reflecting combined influences from differences in land cover representation, initial conditions, and physical parameterizations.

2.4 Model Evaluations

2.4.1 Air Temperature, Humidity, and Wind Speed

To evaluate model performance, we collect temperature, relative humidity, and wind speed from three in-situ observation stations, including a Hadley Centre Integrated Surface Database (HadISD) station (53.354°N, 2.275°W, 2 m) at Manchester airport (Met Office Hadley Centre & National Centers for Environmental Information - NOAA, 2025) (Figure 6(b)), the Manchester Air Quality Supersite (MAQS) station (53.44422°N, 2.21449°W, 7 m) (Watson, 2023b, 2023a) (Figure 6(c)), and the Whitworth station (53.46745°N, 2.23210°W, 53 m) (Centre for Aetmospheric Science - The University of Manchester, n.d.) (Figure 6(d)). These stations measure a range of environments, from rural, through suburban, to urban. Observed variables, recorded at defined heights, are compared with simulated values at the nearest grid cell and matching heights. Specifically, the Whitworth station is used to examine bottom-layer urban atmospheric conditions, while the HadISD and MAQS stations are used for near-surface canopy air conditions.

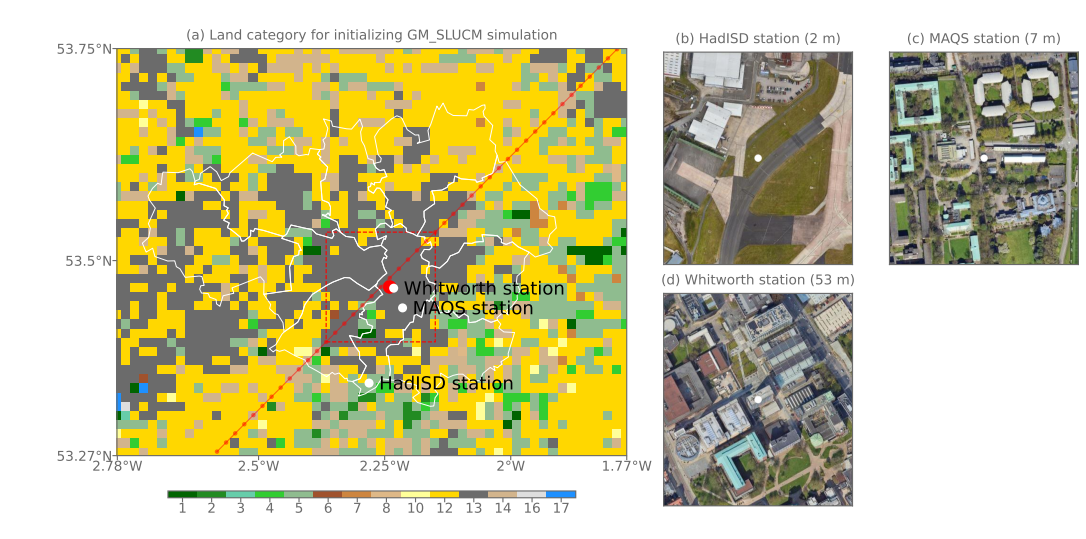


Figure 6. Land surface over Greater Manchester and three in-situ observational stations. (a) Land category for initializing the GM_SLUCM 1.2 km simulation based on the IGBP MODIS dataset. 1: Evergreen needleleaf forest. 2: Evergreen broadleaf forest. 3: Deciduous needleleaf forest. 4: Deciduous broadleaf forest. 5: Mixed forests. 6: Closed shrublands. 7: Open shrublands. 8: Woody savannas. 10: Grasslands. 12: Croplands. 13: Urban and built-up. 14: Cropland/natural vegetation mosaic. 16: Barren or sparsely vegetated. 17: Water. The red rectangle denotes the extent of the main urban area for output analysis. The red dot denotes the location of the city center (53.71048°N, 2.53671°W). The red dashed line denotes the transect used to assess the urban-rural temperature contrast. White dots denote the observation locations. (b) HadISD station (3 m). (c) Manchester Air Quality Supersite (MAQS) station (7 m). (d) Whitworth station (53 m).

2.4.2 Land Surface Temperature

343

344

345

346

347

348

351

352

353

354

355

We compare daytime and nighttime land surface temperature (LST) from simulations with two LST satellite remote sensing products at a spatial resolution of 1 km, including MODIS Aqua satellite data (Wan et al., 2021) and VIIRS data (Hulley & Hook, 2023a, 2023b). This comparison approach has been widely used in previous studies (e.g., Z. Li et al., 2019; Salamanca et al., 2018; X. Zhang et al., 2022). Nevertheless, we treat satellite-derived LSTs as a reference rather than the absolute truth, since they can exhibit systematic biases relative to in-situ measurements (Hu et al., 2014; A. Wang et al., 2014).

The simulated LST in WRF-SLUCM is aggregated from surface temperature (TS) in urban and non-urban fractions (Equation 1):

$$LST = FRC_URB \times TS_URB + (1 - FRC_URB) \times T1, \tag{1}$$

where FRC_URB is the urban fraction (percentage of urban impervious surface) within a grid cell. TS_URB and T1 are surface skin (first-layer) temperature of urban and non-urban surfaces, respectively, calculated using a Newton–Raphson iterative algorithm (Duan et al., 2025).

By contrast, the LST in WRF-CLMU is calculated as (Equation 2):

$$LST = \left(\frac{LW_{up}}{\sigma}\right)^{\frac{1}{4}},\tag{2}$$

where σ is the Stefan-Boltzmann constant (5.67 × 10⁻⁸ W/m² K⁴), and $LW_{\rm up}$ is gridlevel upward longwave radiation aggregated from sub-grid land-units. $LW_{\rm up}$ in CLMU accounts for the surface emissivity. For example, the upward longwave radiation for the roof ($LW_{\rm up-roof}$) is calculated as the sum of the roof emitted longwave and reflected longwave from the atmospheric incoming longwave (Equation 3):

$$LW_{\text{up_roof}} = \epsilon_{\text{roof}} \times \sigma \times \text{TS}_{\text{roof}}^4 + (1 - \epsilon_{\text{roof}}) \times LW_{\text{down}}, \tag{3}$$

where ϵ_{roof} is roof emissivity, TS_{roof} is roof surface temperature, LW_{down} is incoming long-wave from the atmosphere. Combining Equation 2 and 3, the roof radiative temperature (LST_{roof}) is (Equation 4):

$$LST_{roof} = \left(\epsilon_{roof} \times TS_{roof}^4 + \frac{(1 - \epsilon_{roof}) \times LW_{down}}{\sigma}\right)^{\frac{1}{4}}.$$
 (4)

Therefore, LSTs output from WRF-CLMU and WRF-SLUCM differ: the former (Equation 2) represents the effective radiative temperature emitted to the atmosphere, whereas the latter (Equation 1) represents the area-weighted skin temperature within the grid.

We examine daytime and nighttime LST on 16 and 19 July 2022, respectively, the first and hottest days of the record-breaking heatwave period, characterized by continuous energy accumulation and progressive soil moisture depletion. This 4-day heatwave event poses a challenge to the models under extreme conditions. Both NOAH-LSM and CTSM differ not only in their urban modeling but also in how they model non-urban land-units. Focusing on urban climate, we restrict our analysis to grid cells located in the main urban area of the simulation domain, where the urban fraction is high. The city center (53.71048°N, 2.53671°W) is chosen because it exhibits the highest percentage of urban area (88.2%) in GM_CLMU, which is comparable to the constant 100% classified as urban in GM_SLUCM. Note that despite the similar percentage of urban area, the percentage of impervious surface in GM_CLMU is only 44.5%, roughly half of the 90% in GM_SLUCM.

We also analyze LST along a southwest-northeast transect extending from the city center to suburban and rural areas, with the transect direction determined by prevailing wind in July 2022. Due to differences in land cover representation between models, it is not straightforward to directly calculate the surface urban heat island intensity (SUHII) by comparing temperatures between specific urban and rural areas. Instead, a transect-based approach (e.g., Unger et al., 2001; K. Zhang et al., 2010) is adopted to better evaluate each model's ability to capture LST spatial variations and to depict SUHII using maximum and minimum LST along a cross-section.

2.4.3 Surface Energy Fluxes

To understand how models differ in handling urban surface energy balance, we examine radiation, turbulent, and storage heat fluxes from WRF outputs (Equation 5):

$$res = R_{\rm n} - Q_{\rm h} - Q_{\rm le} - Q_{\rm s},\tag{5}$$

where res is residue, Q_s is heat entering the surface, R_n is net radiation flux, Q_h is sensible heat flux, Q_{le} is latent heat flux. For WRF-CLMU simulations with building energy modeling (i.e., GM_CLMU, GM_CLMU_{ALB}), surface energy balance has additional building-related heat fluxes (Equation 6):

$$res = R_{\rm n} + (Q_{\rm ac} + Q_{\rm v} + Q_{\rm w}) - Q_{\rm h} - Q_{\rm le} - Q_{\rm s},$$
 (6)

where $Q_{\rm ac}$ is air-conditioning heat flux, $Q_{\rm v}$ is building ventilation heat flux, $Q_{\rm w}$ is waste heat flux from building space heating and air conditioning.

In WRF-SLUCM, the $R_{\rm n}$ is calculated as (Equation 7):

$$R_{\rm n} = SW_{\rm down} \times (1 - {\rm ALBEDO}) + {\rm EMISS} \times (LW_{\rm down} - \sigma \times {\rm LST}^4),$$
 (7)

where SW_{down} is downward solar radiation, ALBEDO is effective albedo, LW_{down} is downward longwave radiation. EMISS is a constant 0.98 for urban grid cells. Here, EMISS serves as a grid-level surface emissivity used solely for checking the surface energy balance. It is neither the material-based emissivity for roads, roofs, and walls used as model inputs, nor an instantaneous effective emissivity. In WRF-CLMU, the R_n is calculated as (Equation 8):

$$R_{\rm n} = (SW_{\rm down} - SW_{\rm up}) + (LW_{\rm down} - LW_{\rm up}), \tag{8}$$

where $SW_{\rm up}$ is upward solar radiation (reflected by the surface), $LW_{\rm up}$ is upward longwave radiation (surface emitted). Both $SW_{\rm up}$ and $LW_{\rm up}$ are prognostic variables. As EMISS does not play a role in Equation 8, LILAC sets it to 1 merely as a placeholder.

3 Results

406

407

409

410

411

412

413

414

415

416

417

418

419

420

421

422

423

424

428

429

430

3.1 Comparing Model Performance of WRF-CLMU and WRF-SLUCM with In-situ Observations

The simulated monthly mean daily air temperatures at the 2 m or the lowest atmospheric layer in the GM_SLUCM and GM_CLMU simulations generally capture both the magnitude and temporal variability of observations. During summer, the GM_CLMU simulation has higher temperatures than the GM_SLUCM simulation. For example, at the HadISD station, the August mean 2m air temperature (T2M) is 19.0°C in GM_CLMU, 0.4°C higher than in GM_SLUCM, and 0.9°C above the observed value (Figure 7(a)). A similar overestimation occurs at the MAQS station, where GM_CLMU simulates a T2M of 19.5°C, compared to 19.1°C in GM_SLUCM and 19.0°C in the observations (Figure 7(b)). This near-surface warming also affects the temperature at the lowest atmospheric layer (TA). At the Whitworth station, TA is 18.6°C in GM_CLMU, compared to 18.1°C in GM_SLUCM and 17.8°C in observations (Figure 7(c)). By contrast to the summer overestimation, wintertime daily air temperature is slightly underestimated in both simulations compared to observations. For example, at the MAQS station, the observed January mean T2M is 5.5°C, compared to 5.1°C in the GM_CLMU simulation and 4.4°C in the GM_SLUCM simulation. This underestimation of T2M is likely associated with the sensible heat flux $(Q_{\rm h})$. A key contributing factor is the insufficient representation of anthropogenic heat flux in both models. By default, NOAH-SLUCM sets anthropogenic heat flux to 0 W/m²; while CLMU includes only building-related anthropogenic heat, omitting contributions of warming from other sources such as traffic and metabolism.

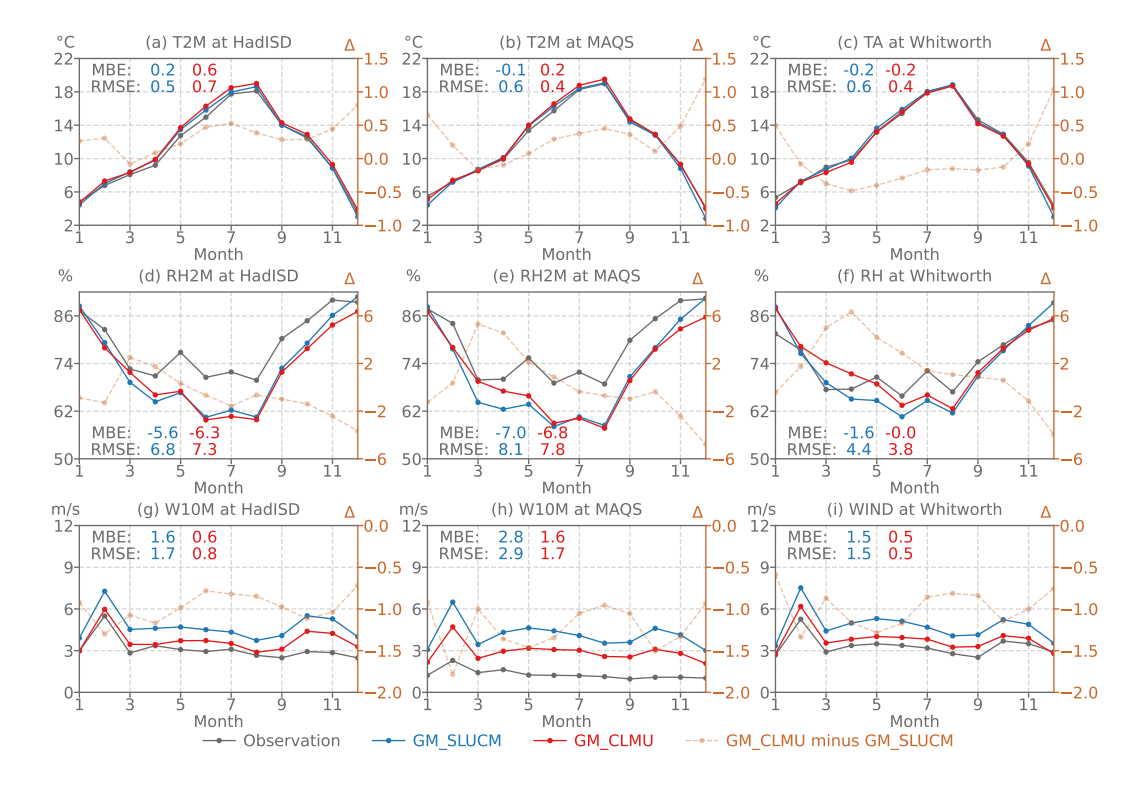


Figure 7. Monthly mean daily 2m air temperature, 2m relative humidity, and 10m wind speed in 2022 at the HadISD and MAQS station, as well as for the lowest atmospheric layer at Whitworth station. T2M and RH2M refer to air temperature and relative humidity at 2 m above the surface, respectively, and W10M refers to wind speed at 10 m. TA, RH, and WIND represent the corresponding values at the lowest atmospheric model level. The left y-axis shows the observed or model variables, while the right y-axis shows the difference (Δ) between the GM_CLMU and GM_SLUCM simulations. Mean bias error (MBE) denotes the mean of the differences between simulations and observations for the whole year, calculated as the monthly mean simulation minus observation. A positive MBE denotes model overestimation, whereas a negative MBE denotes model underestimation. Root mean square error (RMSE) is calculated as the square root of the mean of squared differences between simulations and observations. An RMSE closer to 0 is better.

Both GM_CLMU and GM_SLUCM simulations generally underestimate the monthly mean daily 2m relative humidity (RH2M) at HadISD and MAQS stations, particularly during the summer months. At the HadISD station, the simulated RH2M reaches a minimum in August of 59.9% in GM_CLMU and 60.5% in GM_SLUCM, both lower than the observed value of 69.8% (Figure 7(d)). The underestimated humidity in both models is influenced by the latent heat flux (Q_{le}). According to the Urban-PLUMBER metric results (Lipson et al., 2023), both models exhibit a site-average negative mean bias error (MBE), suggesting that Q_{le} is underestimated compared to observations (Figure A1(d)). However, seasonal reversals occur. For example, at the Whitworth station, GM_CLMU overestimates March and April mean relative humidity at the lowest atmospheric layer (RH) relative to both observations and GM_SLUCM (Figure 7(f)).

Monthly mean daily 10m wind speeds (W10M) in both simulations are higher than the observed, with GM_SLUCM the highest. Previous studies also found overestimation of W10M by NOAH-SLUCM (He et al., 2019; Kadaverugu et al., 2021; Sharma et al., 2017) as well as higher W10M in WRF-SLUCM than in WRF-CLMU4 (Imran et al., 2018).

Local morphological conditions further influence W10M. At the MAQS station, overestimation is likely due to the simplified representation of urban roughness length, with an MBE of 2.8 m/s and 1.6 m/s in the GM_SLUCM and GM_CLMU simulations, respectively (Figure 7(h)). The station, located in a built-up area surrounded by trees, experiences a low monthly mean W10M of around 1.5 m/s, with increased roughness that models do not fully capture. By contrast, the overestimation is more moderate at the HadISD station (Figures 7(g)) and the Whitworth station (Figures 7(i)), both of which have relatively open surroundings and less surface roughness, resulting in higher observed W10M and smaller MBE than at MAQS.

Overall, model performance, evaluated using hourly mean values, varies across different metrics for the three variables (Figure 8). GM_CLMU generally reproduces near-surface wind speed more accurately across the HadISD, MAQS, and Whitworth stations, according to most metrics, except for the correlation coefficient (R). This indicates that, although GM_SLUCM exhibits a larger magnitude bias, its hourly variability aligns more closely with observations. Metrics for T2M at HadISD deviate from the patterns seen at the MAQS and Whitworth stations closer to the city center, where most metrics indicate better performance in the GM_SLUCM simulation. Given the HadISD station near the Manchester Airport, poor performance suggests that GM_CLMU has limited skill in representing sparsely built-up environments compared to GM_SLUCM. GM_CLMU characterizes the HadISD grid cell as 66.4% medium-density urban area based on the 0.05° raw data, which likely overlooks low-density built conditions. By contrast, GM_SLUCM represents HadISD as non-urban, excluding any urban effects.

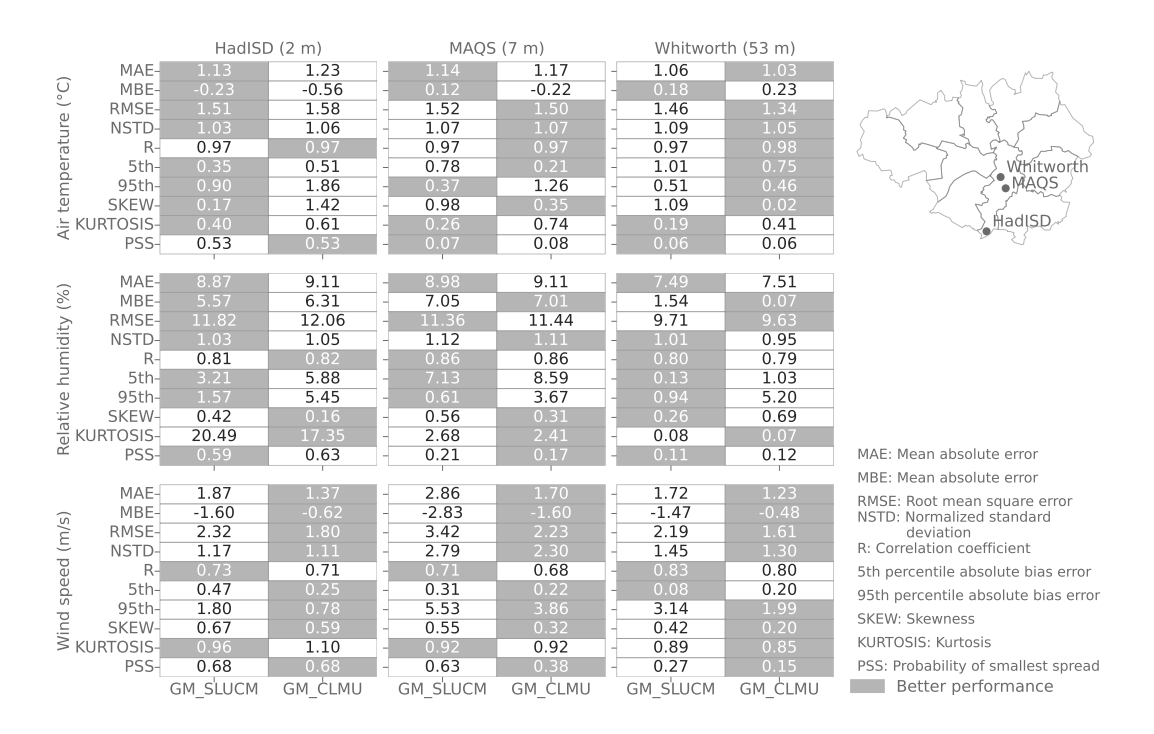


Figure 8. Evaluation of hourly near-surface variables using ten performance metrics from GM_SLUCM and GM_CLMU simulations against observations at HadISD, MAQS, and Whitworth stations. For HadISD and MAQS stations, metrics are based on 2m air temperature, 2m relative humidity, and 10m wind speed, whereas for Whitworth, they are based on variables from the lowest atmospheric layer. Metric definitions follow Lipson et al. (2023). The evaluation is conducted over the full 2022 simulation period, with the spin-up period excluded.

3.2 Comparing Model Performance of WRF-CLMU and WRF-SLUCM with Remote Sensing Products

3.2.1 Spatial Variations of Land Surface Temperature during the 2022 July Heatwave

WRF-CLMU reproduces daytime LSTs with magnitudes and spatial variations that generally align with remote sensing. In the main urban area, GM_SLUCM simulates LSTs around 34–35°C (Figure 9(a)), lower than GM_CLMU reaches by 1–2°C (Figure 9(b)). Observed LSTs exhibit a broader spatial variability, from 30°C to 38°C, effectively capturing both the extreme heat and cooler microclimates. The MODIS map shows a compact area with LSTs peaking at 38°C (Figure 9(d)), while the VIIRS LST map indicates more scattered grid cells reaching 38°C (Figure 9(e)).

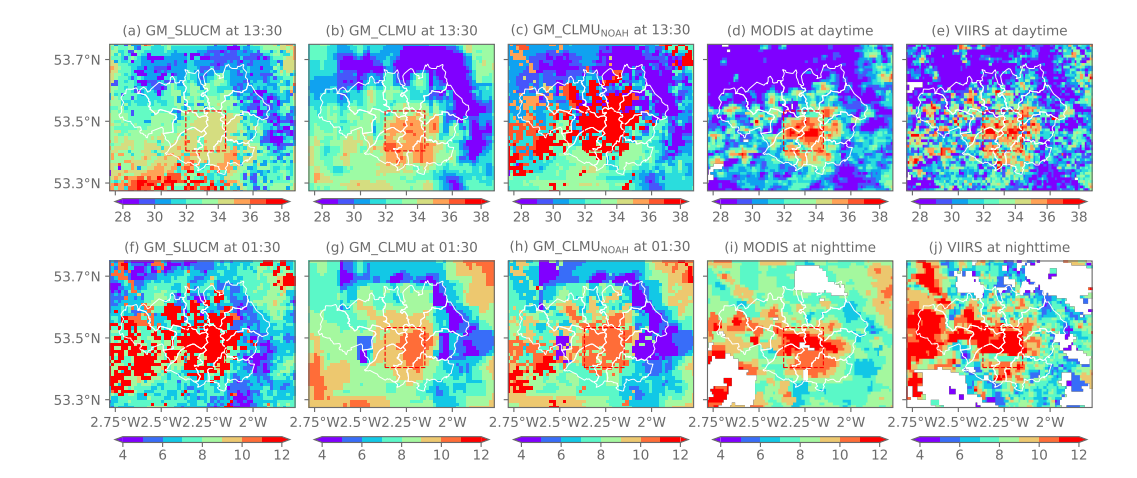


Figure 9. Land surface temperature (LST) from GM_SLUCM, GM_CLMU, and GM_CLMU_{NOAH} simulations (1.2 km), and remote sensing products of the MODIS and VI-IRS (1 km) on 16 July 2022, marking the onset of the July heatwave. (a)–(d) Daytime LST at 13:30 local time. (e)–(h) Nighttime LST at 01:30 local time. White areas in panels for MODIS and VIIRS indicate data removed due to quality control. The red rectangle denotes the extent of the main urban area.

At night, the GM_SLUCM simulation produces LST up to 13°C in the main urban area (Figure 9(f)). The use of dominant land cover type representation results in clearly distinguished LST patterns across grid cells. The GM_CLMU simulation exhibits lower nighttime urban LSTs, with only a few central-city grid cells exceeding 10°C, while surrounding areas remain around 6–10°C (Figure 9(g)). CLMU shows limited spatial variability in LST, likely due to the use of coarse-resolution raw land cover data to generate high-resolution surface input at 1.2 km. This constrains the model's ability to capture fine-scale land surface variations needed for urban climate simulations. The simplification of plant functional types (PFTs) into a single category further reduces surface heterogeneity, contributing to the muted spatial variability. Compared to MODIS LSTs (Figure 9(i)), the VIIRS LST product (Figure 9(j)) detects more distinct high-LST zones in the city core and cooler fringes, showing a strong contrast between urban and rural LSTs.

3.2.2 Model Capability in Depicting Surface Urban Heat Island Intensity

Simulated LSTs differ across both urban and rural areas between the two model configurations, thereby affecting the estimate of urban heat island intensity. Compared to GM_SLUCM, daytime LSTs in GM_CLMU align more closely with observations on 16 July, marking the onset of the heatwave (Figure 10(a)). Along the daytime LST cross-section, the GM_SLUCM and GM_CLMU simulations show daytime gradients of 4.8°C and 9.0°C, respectively, on 16 July. For reference, MODIS shows an LST gradient of 9.0°C between the warmest (36.7°C) and coolest (27.7°C) grid cells. The distance between these two grid cells is about 20.3 km, with the latter located on the northeastern hills. GM_CLMU captures the extreme heat conditions at the city center and the coolest LST over the high-elevation terrain about 20 km to the north, producing a sharper urban—rural contrast. However, both simulations misplace the warm anomaly in the southwest, opposite to the MODIS and VIIRS pattern, introducing additional uncertainty in estimating SUHII across Greater Manchester under extreme heat conditions.

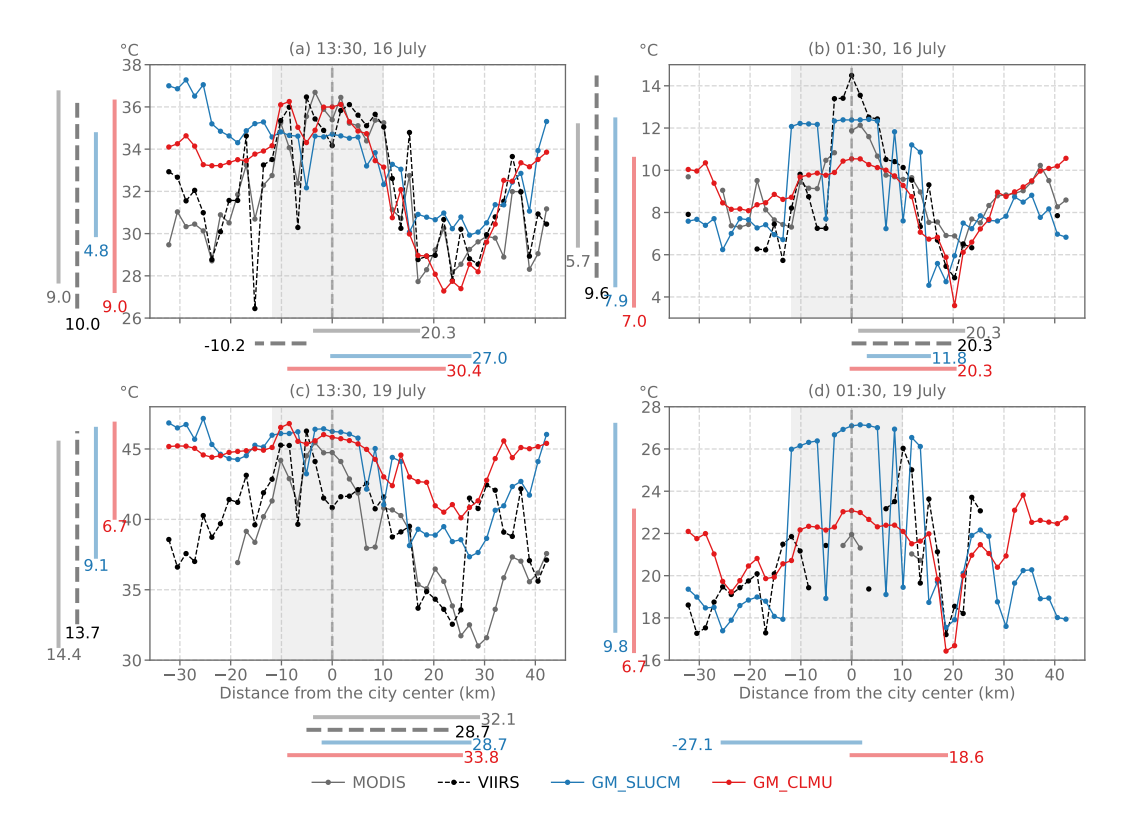


Figure 10. Land surface temperature (LST) along the transect from GM_SLUCM and GM_CLMU simulations, compared with remote sensing products of the MODIS and VIIRS, during the 2022 July heatwave. (a) LST at 13:30 local time, on 16 July. (b) LST at 01:30, on 16 July. (c) LST at 13:30 on 19 July. (d) LST at 01:30 on 19 July. The vertical line at x=0 denotes the city center (53.71048°N, 2.53671°W), with the gray shading indicating the range of the main urban area. Negative values on the x-axis denote locations south of the city center, and positive values denote locations to the north. Maximum LST refers to the highest value within the main urban area. Minimum LST corresponds to the coolest point on the transect. Horizontal lines below the x-axis show the distance (in km) between locations of maximum and minimum LSTs along the transect. Vertical lines to the left of the y-axis show the corresponding temperature gradient (in °C) as the surface urban heat island intensity (SUHII). Maximum and minimum LST values from MODIS and VIIRS for panel (d) are not shown due to excessive missing data.

At night, the GM_CLMU simulation produces a smooth spatial variation pattern of LST (Figure 10(b)). This moderate spatial variation might be a consequence of CLMU's mosaic representation, as values are aggregated from subgrid land-units weighted by their fractional area within each grid cell. However, GM_CLMU underestimates the peak night-time LST at the city center. This underestimation stems from the model configuration, which simplifies urban land cover to a single urban class as a trade-off for computational efficiency. As GM_CLMU only characterizes the urban area as medium density, it fails to capture the characteristics of densely built-up zones with extensive impervious surfaces that store and release heat at night. By contrast, the GM_SLUCM simulation exhibits pronounced LST fluctuations within the main urban area, where built-up surfaces trap heat and remain warm. Due to the use of uniform urban parameters across built-up areas, LST within a 10 km radius of the city center remains similar at 12.2°C, suggesting limited intra-urban variability.

After three days, 19 July experienced the most intense extreme heat conditions. The prolonged accumulation of heat further exacerbates the warming bias in both models. Simulated LST in the main urban area generally rises above 45°C (Figure 10(c)). As the simulated LSTs typically elevate across the region, the temperature gradient between the maximum and minimum LST along the cross-section narrows to 6.7°C in the GM_CLMU simulation. This gradient is lower than the corresponding values of 9.1°C in the GM_SLUCM simulation, 13.7°C in VIIRS, and 14.4°C in MODIS. The underestimated temperature gradient in GM_CLMU and GM_SLUCM is primarily due to the overestimated LSTs in rural areas. Both models exhibit weaker vegetation cooling effects and thereby pose uncertainties for depicting SUHII under extreme heat conditions.

Despite similar daytime LSTs around 46°C in the main urban area, nighttime LSTs in the GM_CLMU simulation drop to 22–23°C, while in the GM_SLUCM simulation remain 27°C (Figure 10(d)). At the city center, nighttime LST in GM_CLMU is closer to the MODIS-based LST of 22°C, whereas simulated LSTs in GM_SLUCM for grid cells 10 km north of the city center agree better with VIIRS-based values. The larger daynight LST difference in the GM_CLMU simulation indicates faster urban nocturnal cooling compared to GM_SLUCM.

3.2.3 Surface Energy Balance Explanation of Model Differences

During the July heatwave, GM_CLMU produces a warmer, drier, and less windy daytime urban environment compared to GM_SLUCM, whereas the opposite pattern emerges at night. These differences mainly result from the energy partition between turbulent heat and storage heat. At the city center, the mean daytime storage heat flux (Q_s) in the GM_SLUCM simulation is 145.2 W/m², while Q_{le} is 3.9 W/m² (Figure 11(a)). The proportion of sensible, latent, and storage heat is 58.9%, 0.8%, and 40.3%, respectively. According to WRF's default look-up table of urban parameters, grid cells dominated by urban only have a 10% vegetation (pervious-surface) fraction, which contributes to the low moisture flux (Patel et al., 2022). In the main urban area, the daytime Q_s is 134.0 W/m², lower than the Q_s from the city center (Figure 11(c)). That is, the main urban area has some non-urban grid cells, which exhibit less energy storage in the soil and more in turbulent fluxes.

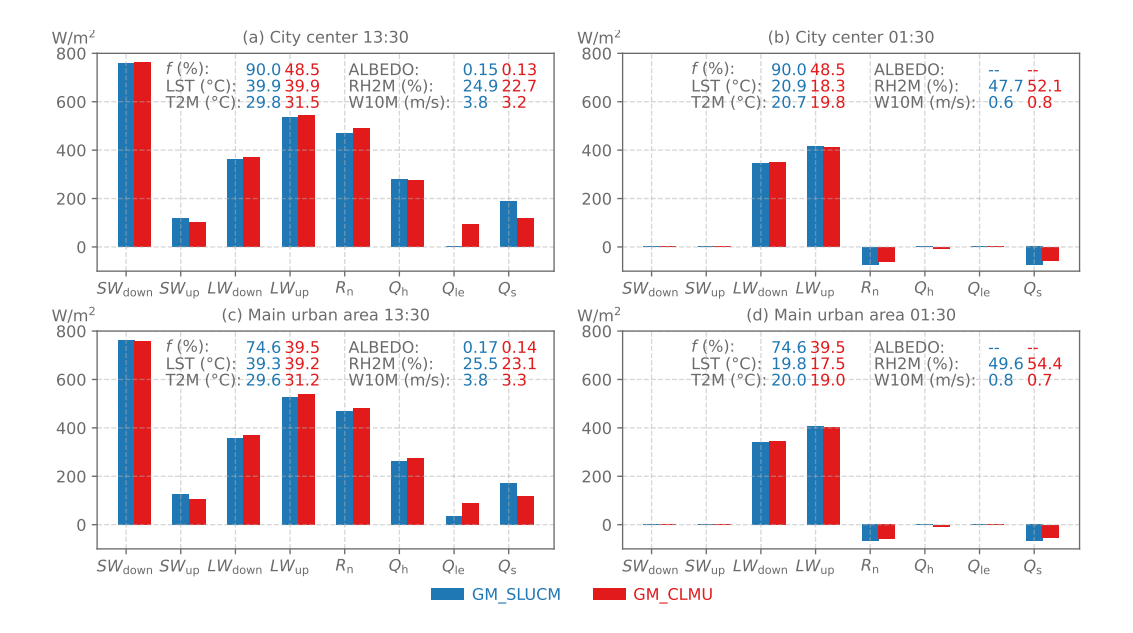


Figure 11. Average urban surface fluxes in the GM_SLUCM and GM_CLMU simulations during a heatwave of 16–19 July 2022. (a) and (b) City center (the grid cell of 53.71048°N, 2.53671°W). (c) and (d) The main urban area (grid cells within the rectangle domain). $SW_{\rm down}$ is downward solar radiation. $SW_{\rm up}$ is upward solar radiation. $LW_{\rm down}$ is downward longwave radiation. $LW_{\rm up}$ is upward longwave radiation. $R_{\rm n}$ is net radiation ($R_{\rm n} = SW_{\rm down} + LW_{\rm down} - SW_{\rm up} - LW_{\rm up}$). $Q_{\rm h}$ is sensible heat flux. $Q_{\rm le}$ is latent heat flux. $Q_{\rm s}$ is the flux going into the ground, as storage heat flux. f denotes the percentage of the urban area covered by impervious surfaces. ALBEDO is the instantaneous effective albedo (ALBEDO = $\frac{SW_{\rm up}}{SW_{\rm down}}$). LST is the land surface temperature. T2M is the 2m air temperature. RH2M is the 2m relative humidity. W10M is the 10m wind speed.

By contrast, the GM_CLMU simulation represents a much larger fraction of pervious canyon floor, corresponding to areas with urban vegetation. This results in a greater portion of available energy being partitioned into latent heat flux (Q_{le}) , with the day-time surface energy budget distributed as 57.1% sensible heat, 18.9% latent heat, and 24.0% storage heat. Despite the larger pervious floor fraction, GM_CLMU produces a higher daytime 2-m air temperature (31.5 °C), 1.7 °C warmer than GM_SLUCM (29.8 °C). This apparent inconsistency arises because CLMU simplifies the associated physical processes for the pervious floor by a bulk soil representation and does not explicitly represent urban vegetation transpiration. Under extreme heat conditions, such as heatwaves, the reliance on a bulk soil model may further reduce the simulated cooling effect, depending on soil moisture availability.

At night, both models exhibit negative Q_s , indicating that heat is released from the ground to the atmosphere. Since CLMU simulates a lower Q_s during the day, the magnitude of nighttime ground heat release is also smaller (Figure 11(b), (d)). Accordingly, T2M at the city center is 19.8°C in GM_CLMU, 0.9°C lower than in GM_SLUCM of 20.7°C. Alongside temperature reduction, nighttime RH2M and W10M are higher in GM_CLMU. These three variables, T2M, RH2M, and W10M, influence heat impact assessment, such as human heat stress (Buzan et al., 2015).

3.3 WRF-CLMU Sensitivity to Urban Parameters

568

569

570

571

572

573

574

575

577

578

579

580

581

582

584

585

586

587

588

589

Given that WRF-CLMU tends to simulate warmer daytime and cooler nighttime near-surface air temperatures on a monthly mean basis, we primarily attribute this to differences in urban parameters, for example, albedo, as it governs surface energy absorption, and, in turn, modulates energy fluxes (e.g., sensible and latent heat fluxes) and diagnostic variables such as temperature. Urban-PLUMBER results further indicate that CLMU5 under the baseline experiment (using model-specific parameters) overestimate $Q_{\rm h}$ and underestimate $SW_{
m up}$, as reflected by a positive 20-site average MBE for $Q_{
m h}$ (Figure A1(c)) and a negative MBE for SW_{up} (Figure A1(a)). GM_SLUCM and GM_CLMU simulations prescribe different albedo values as input. GM_SLUCM uses a uniform default value of 0.2 for roofs, walls, and roads, whereas GM_CLMU assigns similar albedo values for roofs (0.23) and walls (0.27), but notably lower values for impervious floor (0.13)and pervious floor (0.08) (Table B1). As a result, GM_SLUCM and GM_CLMU simulate instantaneous albedo values of 0.15 and 0.13, respectively, at 13:30 during 16-19 July at the city center (Figure 12(a)). In winter, however, differences in prescribed albedo have minimal effect, with both GM_SLUCM and GM_CLMU producing similar effective albedo values of 0.15 during 4–6 January (Figure 12(c)). The impact of urban surface reflection in winter is reduced due to weak incoming solar radiation in high-latitude urban areas like Greater Manchester.

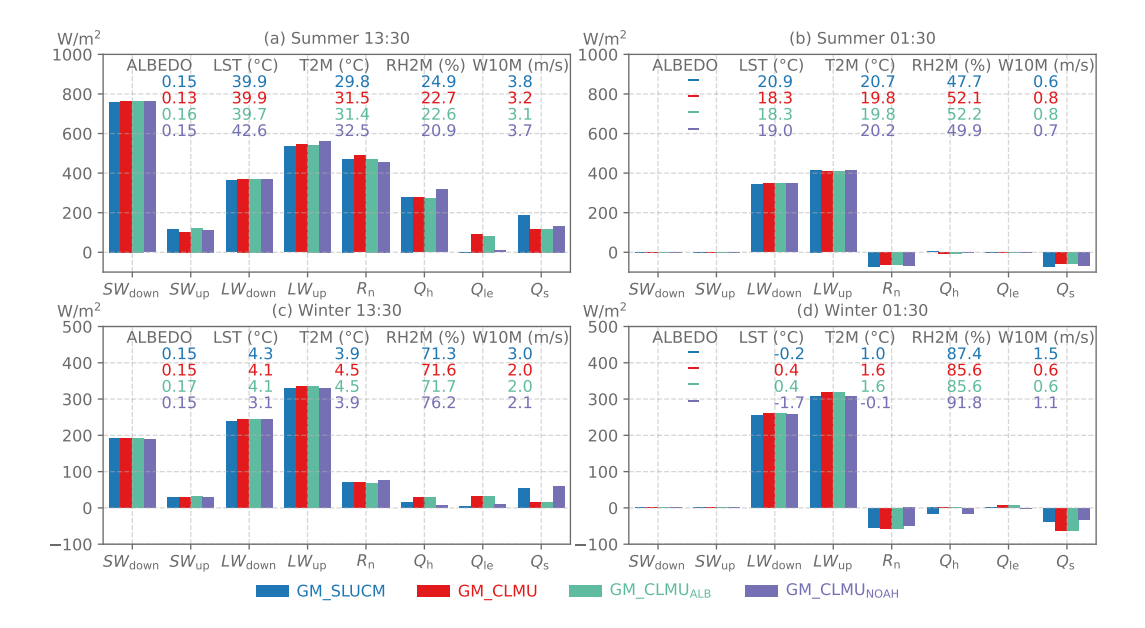


Figure 12. Average urban surface fluxes at the city center (the grid cell of 53.71048°N, 2.53671°W). (a) and (b) During 16–19 July. (c) and (d) During 4–6 January 2022. $SW_{\rm down}$ is downward solar radiation. $SW_{\rm up}$ is upward solar radiation. $LW_{\rm down}$ is downward longwave radiation. $LW_{\rm up}$ is upward longwave radiation. $R_{\rm n}$ is net radiation ($R_{\rm n} = SW_{\rm down} + LW_{\rm down} - SW_{\rm up} - LW_{\rm up}$). $Q_{\rm h}$ is sensible heat flux. $Q_{\rm le}$ is latent heat flux. $Q_{\rm s}$ is the flux going into the ground, as storage heat flux. ALBEDO is the instantaneous effective albedo (ALBEDO = $\frac{SW_{\rm up}}{SW_{\rm down}}$). LST is the land surface temperature. T2M is the 2m air temperature. RH2M is the 2m relative humidity. W10M is the 10m wind speed.

When the albedo of both impervious floor and pervious floor is increased to 0.23, GM_CLMU_{ALB} produces only a slightly higher effective albedo by 0.03 in summer (0.16 vs. 0.13 for GM_CLMU) (Figure 12(a)) and 0.02 in winter (0.17 vs. 0.15 for GM_CLMU)

591

592

595

596

597

598

599

601

602

603

606

607

608

610

611

612

614

615

616

617

618

619

620

621

622

623

626

627

628

629

630

(Figure 12(c)). Albedo perturbation results in a minimal reduction of net radiation in GM_CLMU_{ALB}. Consequently, surface energy fluxes remained largely unchanged, and diagnostic variables (i.e., LST, T2M, RH2M, W10M) show limited sensitivity to road albedo perturbation. The mean daytime T2M only decreases by 0.1°C from 31.5°C in GM_CLMU to 31.4°C in GM_CLMU_{ALB}, still higher than 29.8°C in GM_SLUCM. This outcome aligns with previous findings that road-albedo modifications generally have smaller cooling effects than increasing roof-albedo modifications, owing to the constraint imposed by urban morphology and model physics (Y. Sun et al., 2024). In terms of urban forms, the canyon height-to-width ratio and building height influence radiation reflection and sensible heat. In particular, GM_CLMU represents taller buildings (15 m) compared to GM_SLUCM (7.5 m), likely to increase sensible heat and amplify canopy-layer air temperature.

When all urban morphological, radiative, and thermal parameters are set to match those in the GM_SLUCM simulation, $GM_{-}CLMU_{NOAH}$ simulation shows increases in daytime storage heat flux (Q_s) compared to GM_CLMU and GM_CLMU_{ALB} simulation, due to a reduction of pervious floor fraction from 45% to 0% (Figure 12(a), (c)). Without any pervious floor, GM_CLMU_{NOAH} simulates a daytime LST of 42.6°C during 16–19 July, 2.7°C higher than in GM_SLUCM (39.9°C). Increasing the impervious surface fraction to 90% raises not only daytime but also nighttime LST (Figure 9(c), (h)), resulting in values more comparable to remote-sensing-based LSTs. Such a warmer phenomenon in GM_CLMU_{NOAH} does not occur in winter as the simulation turns off building space heating. During 4–6 January, LST at 13:30 in GM_CLMU_{NOAH} is 1.2°C lower than in GM_SLUCM, yet the two simulations produce the same T2M (Figure 12(c)). This suggests that, under identical urban parameters, variations in model physics or respective initial conditions may influence the results. At 01:30, surface fluxes between GM₋CLMU_{NOAH} and GM_SLUCM are rather similar, but the diagnostic variables such as LST and T2M are still different (Figure 12(d)). Nighttime T2M of 1.7°C in GM_CLMU_{NOAH} is 2.1°C lower than in GM_CLMU (0.4°C). CLMU is highly sensitive to anthropogenic heat for urban regions under cold background climate conditions, which constitutes the dominant source of urban warming at night. By contrast, without incorporating any anthropogenic heat, GM_SLUCM remains warmer throughout the day and night.

The atmospheric component responds to seasonal variations induced by urban surfaces. At the city center at 13:30, the bottom atmospheric layer sees the highest summer daytime TA in the GM_CLMU_{NOAH} simulation, followed by GM_CLMU, GM_CLMU_{ALB}, and GM_SLUCM (Figure 13(a)). The lowest TA in the GM_SLUCM simulation mainly results from its comparatively low T2M. On summer nights, all WRF-CLMU simulations show lower TAs compared to GM_SLUCM, with the maximum difference (Δ TA) reaching -1.5° C (Figure 13(b)). Wintertime TAs are less influenced by urban variations, where Δ TAs vary from -0.3° C to 0.2° C among simulations during the day (Figure 13(c)), and from -0.4° C to 0.2° C at night (Figure 13(d)). Differences in TAs diminish across the bottom layers, while a reverse pattern emerges aloft.

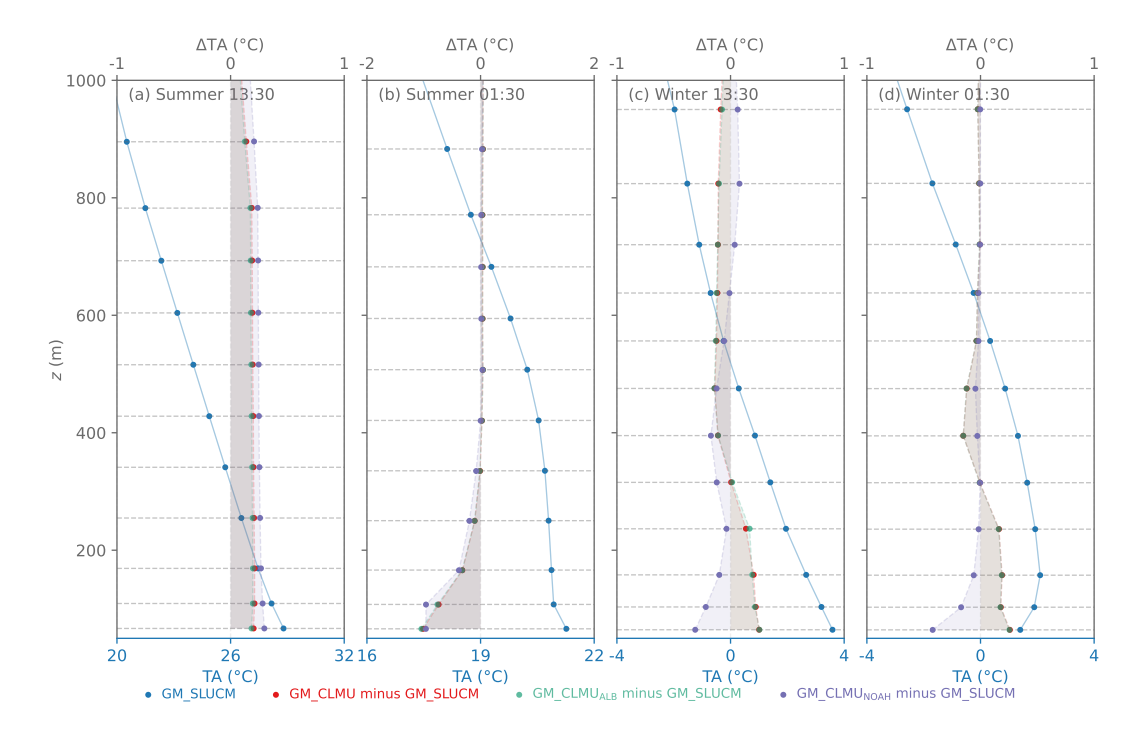


Figure 13. Average atmospheric temperature (TA) at the city center (the grid cell of 53.71048°N, 2.53671°W). (a) and (b) 16–19 July 2022. (c) and (d) 4–6 January 2022. TA on the bottom x-xais denotes values from the GM_SLUCM simulation. Δ TA on the top x-xais denotes values of GM_CLMU or GM_CLMU_{ALB} or GM_CLMU_{NOAH} minus GM_SLUCM. z denotes a certain geopotential height above mean sea level.

4 Conclusion

This study demonstrates the capability of the Community Land Model-Urban (CLMU) via WRF coupling for high-resolution urban climate simulations. Being coupled to an active atmospheric model, the need for externally prepared forcing data in CLMU is removed, allowing for online simulations with dynamic downscaling. We take Greater Manchester (GM), UK, as a testbed to compare the performance of WRF's embedded NOAH single-layer urban canopy model (WRF-SLUCM) against WRF-CLMU. These two atmosphereland coupled simulations, GM_SLUCM and GM_CLMU, use four nested domains, with the innermost grid spacing of 1.2 km.

Results show that both simulations perform comparably, with monthly mean near-surface air temperature closely matching observations at three in-situ stations. A heat-wave event (16–19 July 2022) is further analyzed to assess model performance in simulating land surface temperature (LST). On the onset of the July heatwave, GM_CLMU simulates the daytime LSTs by 1–2°C higher than GM_SLUCM in urban areas, better capturing extreme heat conditions. GM_CLMU reproduces a daytime surface urban heat island intensity (SUHII) of 9.0°C along a southwest-northeast transect, closely matching remote-sensing-based estimates. By contrast, it underestimates nighttime LSTs in urban areas, with values up to 4°C lower than satellite products. On 19 July, the peak of the heatwave, both models show a daytime warming bias under extreme heat conditions. Elevated simulated LSTs in both urban and rural areas result in lower SUHII (9.1°C in GM_SLUCM and 6.7°C in GM_CLMU) than observed by satellites (14.4°C in MODIS and 13.7°C in VIIRS).

As CLMU and SLUCM are fundamentally distinct, output variations arise from multiple factors, including model physics, initial conditions, land cover classification, and the parameters used to represent land properties. For example, the GM_SLUCM simulation produces a narrower diurnal temperature range with lower daytime temperature and higher nighttime air temperature compared to the GM_CLMU simulation. Modelspecific parameters partially determine this behavior, one of which is the pervious surface fraction. As the default setting of the proportion of pervious surface of 10%, the GM_SLUCM simulation partitions more heat into ground flux during the day. Comparatively, the GM_CLMU simulation represents a larger pervious floor fraction (45%), which partitions less energy into storage heat and more into turbulent heat fluxes. However, CLMU parameterizes the pervious floor through a bulk soil model that does not account for transpiration from urban trees. This simplification may constrain its performance under extreme heat events, such as heatwaves, when cooling is further moderated by soil moisture limitations. In addition, sensitivity tests show that increasing the prescribed road albedo by 0.1 only increases effective albedo by 0.02-0.03 in the WRF-CLMU_{ALB} simulation, and does not significantly influence the simulated thermal conditions. Substituting all GM_SLUCM parameters into CLMU notably increases daytime storage heat fluxes in GM_CLMU_{NOAH} and thereby increases LST.

We acknowledge that the performance of urban climate modeling may vary across different urban areas, influenced by variations in urban land cover classification and corresponding parameters. Since the main objective of this study is to demonstrate the capability of WRF-CLMU for regional urban climate simulations, we do not distinguish the differences between WRF-CLMU and WRF-SLUCM through point-to-point control experiments. Our findings are case-specific, and additional testbeds are required to evaluate model performance under varying background climates and urban parameters. For instance, an ensemble approach (e.g., Imran et al., 2018) could be used to assess climate dynamics with WRF-CLMU, considering uncertainties from different atmospheric schemes or variations in land initial conditions. As the urban model of the CESM, CLMU relies on default land surface input derived from coarse-resolution raw data. This limits CLMU's ability to represent urban land cover heterogeneity when interpolated to kilometer-scale grids and reduces its capability to capture microclimatic variations under extreme conditions. The future applications of WRF-CLMU in urban climate studies stand to benefit from more detailed representations of urban land cover, such as those based on local climate zone classification (Y. Sun, Oleson, Zhao, et al., 2025) or high-resolution urban parameter datasets (e.g., Cheng et al., 2025; L. Li et al., 2024; Liao et al., 2025). Building on our baseline case study, future investigations using WRF-CLMU with refined model configurations and calibration are expected to further improve our understanding of model behaviors.

Appendix A Model Intercomparisons

653

654

658

659

661

662

665

666

667

669

670

671

672

673

674

677

678

679

680

681

682

685

686

687

689

690

691

692

693

697

698

699

701

702

703

A1 Results from the Urban-PLUMBER Project

The Urban-PLUMBER conducted two experiments: the baseline one using default model parameters, and the detailed one using the provided parameters, providing evidence for model evaluation between CLMU5 and NOAH-SLUCM in single-point land-only mode. The baseline results suggest that uncertainties stem from both model physics and urban parameters, whereas the detailed results point to differences mainly attributed to model physics.

The mean bias error (MBE) between observed and simulated upward longwave radiation ($LW_{\rm up}$) indicates a general overestimation in both models, with NOAH-SLUCM producing higher MBEs than CLMU5 at most flux tower sites (Figure A1(b)). Latent heat flux ($Q_{\rm le}$) from both models appears insensitive to parameter differences between the baseline and detailed experiments, as reflected by the similar MBE values in both

cases (Figure A1(d)). Negative MBE for $Q_{\rm le}$ is likely due to a lack of explicit urban vegetation modeling. In the baseline experiment, site-average MBE for sensible flux $(Q_{\rm h})$ is $4.7\pm19.1~{\rm W/m^2}$ and $-8.6\pm23.0~{\rm W/m^2}$ in CLMU5 and NOAH-SLUCM, respectively, indicating a greater overestimation of $Q_{\rm h}$ by CLMU5 using model default parameters (Figure A1(c)). When local parameters are applied, this bias is reduced. The site-average MBE for $Q_{\rm h}$ in CLMU5 decreases from $4.7\pm19.1~{\rm W/m^2}$ to $-2.6\pm16.0~{\rm W/m^2}$.

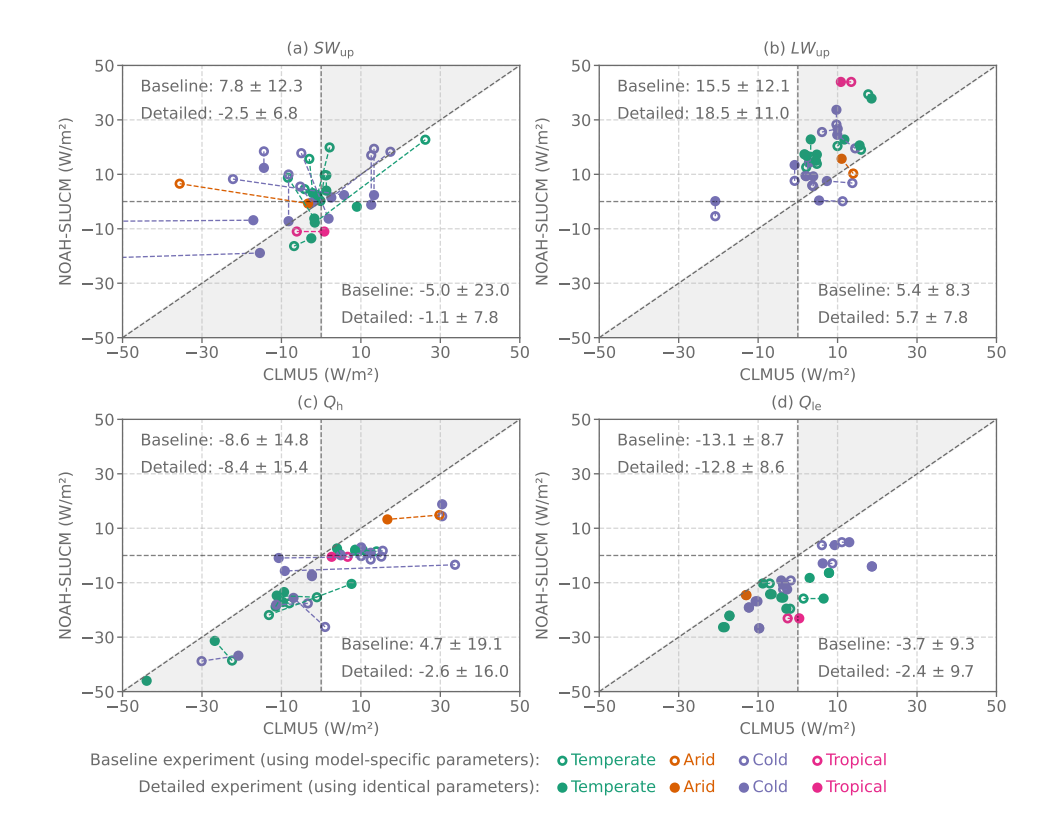


Figure A1. Mean bias error (MBE) between the simulated and observed (a) upward solar radiation ($SW_{\rm up}$), (b) upward longwave radiation ($LW_{\rm up}$), (c) sensible heat flux ($Q_{\rm h}$), and (d) latent heat flux ($Q_{\rm le}$) over 21 urban flux tower sites. Metric data came from the Urban-PLUMBER project (https://urban-plumber.github.io/, last access: 26 November 2025) (Lipson et al., 2021), with baseline and detailed experiments using different parameters (Lipson et al., 2023). Sites are classified by the Köppen-Geiger climate zone system to indicate background climate conditions. MBE >0: Model is overestimating on average. MBE < 0: Model is underestimating on average. The top-left texts in each panel indicate the site-average MBE for NOAH-SLUCM, while the bottom-right texts show the MBE for CLMU5.

A2 Turbulent Heat Transfer

NOAH_SLUCM and CLMU are different in turbulent heat transfer from urban surfaces to the atmosphere. Taking sensible heat as an example, NOAH_SLUCM calculates sensible heat flux (Q_h) as (Equation A1):

$$Q_{h} = FLXTH \cdot \rho_{atm} \cdot c_{p}, \tag{A1}$$

where c_p is the specific heat capacity of air, $\rho_{\rm atm}$ is air density at the first atmospheric level. FLXTH is the potential temperature flux aggregated from roof, wall, and road with

areal weights, calculated as (Equation A2):

$$FLXTH = R \cdot FLXTH_{roof} + W \cdot FLXTH_{wall} + RW \cdot FLXTH_{road}, \tag{A2}$$

where FLXTH_{*} denotes the potential temperature flux of a certain urban surface (i.e., roof, wall, road). R is roof width, W is wall width, and RW is road width. FLXTH_{*} is calculated as (Equation A3):

$$FLXTH_* = \frac{Q_{h,*}}{\rho_{atm} \cdot c_p},\tag{A3}$$

where $Q_{\rm h,}$ * denotes the sensible heat flux on a certain urban surface (i.e., HR, HB, HG). Roof directly interacts with the bottom atmosphere, with roof sensible heat flux ($Q_{\rm h, roof}$) calculated as (Equation A4):

$$Q_{\text{h.roof}} = \rho_{\text{atm}} \cdot c_p \cdot \text{CH}_{\text{roof}} \cdot \text{U}_{\text{atm}} \cdot (\theta'_{\text{roof}} - \theta_{\text{atm}}), \tag{A4}$$

where CH_{roof} denotes the heat transfer coefficient for the roof, U_{atm} is the wind speed at the first atmospheric level, θ_{atm} is the potential temperature at the first atmospheric level, θ'_{roof} is the roof potential temperature at previous time step. By contrast, the wall and road directly interact with the canopy air at the zero-plane displacement height level. For instance, wall sensible heat flux $(Q_{h, wall})$ is calculated as (Equation A5):

$$Q_{\text{h,wall}} = \rho_{\text{atm}} \cdot c_p \cdot \text{CH}_{\text{wall}} \cdot \text{U}_{\text{canopy}} \cdot (\theta'_{\text{wall}} - \theta_{\text{canopy}}), \tag{A5}$$

where U_{canopy} and θ_{canopy} are wind speed and potential temperature at the urban canopy level.

CLMU assumes that all surfaces interact with canopy air while canopy air interacts with the bottom atmosphere. That is, CLMU calculates Q_h as (Equation A6):

$$Q_{h} = \rho_{\text{atm}} \cdot c_{p} \cdot \frac{1}{r_{\text{atm-canopy}}} \cdot (\theta_{\text{canopy}} - \theta_{\text{atm}}),$$

$$= \rho_{\text{atm}} \cdot c_{p} \cdot \frac{1}{r_{\text{canopy-*}}} \cdot \sum w_{*} \cdot (\theta_{*} - \theta_{\text{canopy}})$$
(A6)

where $r_{\text{atm-canopy}}$ is aerodynamic resistance for sensible heat transfer between urban canopy air and the atmosphere. $r_{\text{canopy-*}}$ is the aerodynamic resistance for sensible heat transfer between a certain urban surface (i.e., roof, sunlit wall, shaded wall, pervious floor, and impervious floor) and canopy air. w_* is the surface areal weight. CLMU uses θ_{canopy} to represent 2m air temperature (T2M).

A3 Model Vertical-layer Configuration

WRF treats the land surface layer as a constant flux layer, about 0.1 of the planetary boundary layer ($Z_{\rm sl} \approx 0.1 \cdot Z_{\rm pbl}$) (Skamarock et al., 2019). For single-layer urban canopy models like NOAH-SLUCM and CLMU, variables at the lowest atmospheric level (k=1) are used to derive surface heat and moisture fluxes based on Monin–Obukhov Similarity Theory (Monin & Yaglom, 2013). In NOAH-SLUCM, the urban canopy layer is located lower than the roof. The lowest atmospheric layer must be located above the sum of canopy displacement height ($Z_{\rm d}$), canopy roughness length ($Z_{\rm 0}$), and an additional 2 m buffer ($Z_{\rm 1} > Z_{\rm d} + Z_{\rm 0} + 2$), to ensure numerical stability (Figure A2).

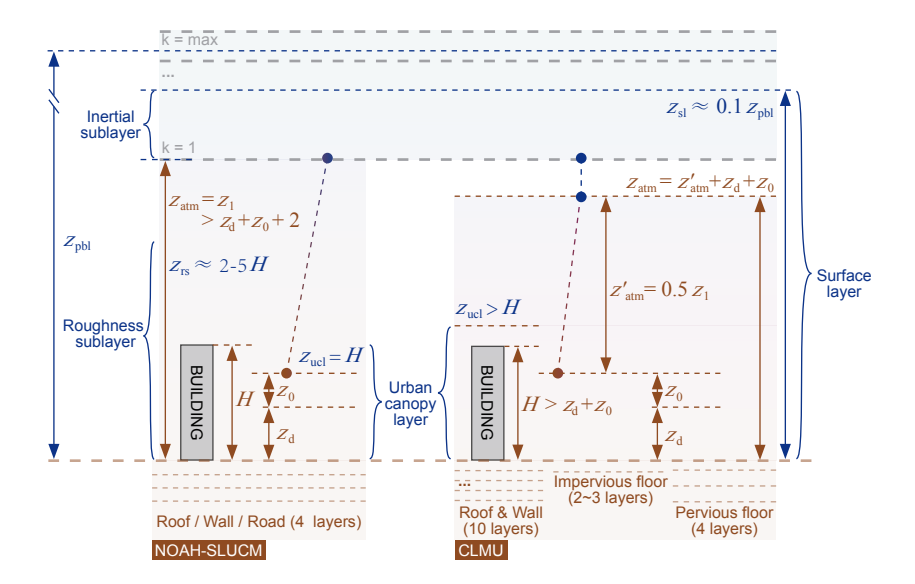


Figure A2. Cross-sectional schematic of atmosphere-urban coupling in WRF-SLUCM and WRF-CLMU. $Z_{\rm pbl}$ is the height of the planetary boundary layer. $Z_{\rm sl}$ is the height of the surface layer. $Z_{\rm 1}$ is the height of the bottom atmospheric layer (k=1). $Z_{\rm atm}$ is the height of atmospheric forcing for urban canopy models. H is the average building height. $Z_{\rm 0}$ is the canopy roughness length. $Z_{\rm d}$ is the canopy displacement height. $Z'_{\rm atm}$ is the reference height of the atmosphere. $Z_{\rm atm}$ is atmospheric forcing height. This simplified diagram illustrates the placement of the single-layer urban canopy models beneath the atmosphere. Meyer et al. (2020) and Schoetter et al. (2020) has provided relevant explanations of the relationships between surface representations in the atmospheric model and those in the urban model.

By contrast, CLMU does not require the bottom atmospheric layer height. According to the code that imports WRF variables at the lowest atmospheric level to CLMU (https://github.com/wrf-model/WRF/blob/master/phys/module_sf_ctsm.F, last access: 26 November 2025), LILAC defines the reference atmospheric height ($Z'_{\rm atm}$) as the midpoint of the lowest atmospheric layer (Z_1). Consequently, the atmospheric forcing height ($Z_{\rm atm}$) used for flux computation is the sum of $Z'_{\rm atm}$, $Z_{\rm d}$, and Z_0 ($Z_{\rm atm} = Z'_{\rm atm} + Z_{\rm d} + Z_0$). CLMU explicitly resolves the canopy-layer air space through resistance-based formulations, including surface resistance and aerodynamic resistance. The canopy layer is located above the roof. In addition, CLMU performs a hard-coded check that the average building height (H) exceeds the sum of $Z_d + Z_0$, i.e., $H > Z_d + Z_0$. If this condition is not met, the model initialization is terminated with an error.

Appendix B Analysis of Greater Manchester Simulations

B1 Inputs

Table B1 lists the default urban parameters used for GM_SLUCM and GM_CLMU simulations.

Table B1. List of Urban Parameters for GM_SLUCM and GM_CLMU Simulations.

Attribute	Name of parameter	GM_SLUCM	$\mathrm{GM}_{-}\mathrm{CLMU}$	\mathbf{Unit}	
	Canyon height to width ratio	0.8	0.75	Unitless	
Morphological	Height of roof	7.5	15	meter	
	Thickness of roof	0.2	0.15	meter	
	Thickness of wall	0.2	0.28	meter	
	Fraction of roof	0.5	0.35	Unitless	
	Fraction of impervious floor	0.5	0.2	Unitless	
	Fraction of pervious floor	_	0.45	Unitless	
	Albedo of impervious floor	0.2	0.13	_	
	Albedo of pervious floor	_	0.08		
	Albedo of roof	0.2	0.23	_	
Radiative	Albedo of wall	0.2	0.27	– – Unitless	
radiative	Emissivity of impervious floor	0.95	0.91	- Unitiess	
	Emissivity of pervious floor	_	0.95	_	
	Emissivity of roof	0.9	0.9	-	
	Emissivity of wall	0.9	0.91	_	
	Volumetric heat capacity of impervious floor	1000	[2060.5, 1712.3]	kJ/m³ K	
Thermal	Volumetric heat capacity of roof	1000	[1700, 1200, 9940, 1200, 1200, 1200, 1010, 1010, 1010, 6090]	- ′	
	Volumetric heat capacity of wall	1000	[1520.7, 1520.7, 138.1, 919.3, 773, 773, 773, 225.7, 194.4, 621.4]	_	
	Thermal conductivity of impervious floor	0.4004	[1.67, 0.56]		
	Thermal conductivity of roof	0.67	[1.2, 0.03, 0.15, 0.03, 0.03, 0.03, 0.04, 0.04, 0.04, 0.16]	W/m K	
	Thermal conductivity of wall	0.67	[2.5, 2.5, 0.14, 2.1, 0.67, 0.67, 0.67, 1.6, 2.2, 2.3]	_	
Indoor	Maximum building interior temperature Minimum building interior temperature	Not applicable Not applicable	99.95 16.95	- °C	

NOAH-SLUCM sets 4 urban surface layers, with uniform thermal parameters across layers. CLMU sets 10 layers, with thermal parameters varying with layers based on construction materials, reflecting depth-dependent material properties (Jackson et al., 2010). This allows CLMU to capture vertical heat storage and release more realistically than a simple average.

B2 CTSM Configuration

761

762

763

CTSM fast configuration simplifies land representation to save computation (Table B2).

 $^{^2\,}$ In the GM_CLMU simulation, there are 2 layers for impervious floor, and the rest are soil.

³ In GM_CLMU, setting the minimum building air temperature to 16.95°C means that space heating is calculated only when the indoor temperature falls below 16.95°C. Similarly, setting the maximum building air temperature to 99.95°C effectively disables the calculation of air conditioning flux.

Table B2. Name-list of Model Configuration for WRF-CLMU.

Configuration	Long name	standard	fast	Influence on urban climate simulation
soil_layerstruct_predefinedSoil layers and depth		20-layer soil column, 8 m of soil, 5 bedrock layers	4-layer soil column, 2 m of soil, 0 bedrock layers	Energy and water processes on urban pervious floor
itmax_canopy_fluxes	Maximum number of iterations used for canopy fluxes	40	3	Urban canopy thermal conditions
nlevsno	Number of snow layers	12	5	Urban snow and related hydrologic processes
h2osno_max	Maximum snow depth in H2O equiva- lent	10000.0 mm	5000.00 mm	Urban snow and related hydrologic processes
collapse_urban	Represent urban land cover by a dom- inant urban land-unit	.false.	.true.	Representation of urban land cover heterogeneity
n_dom_landunits	Represent land cover by a dominant land-unit	.false.	.true.	Representation of urban areal fraction
n_dom_pfts	Number of dominant plant functional types (PFTs)	0 (Using all PFTs)	1 (Using 1 PFTs)	No direct impacts on urban areas, but indirectly influences urban-rural climate contrast through changes in rural land representation

¹ This table refers to the default name-list for building CTSM, defined in https://github.com/ESCOMP/CTSM/blob/master/bld/namelist_files/namelist_defaults_ctsm.xml (last access: 26 November 2025).

B3 Outputs

765

Table B3 lists variables for analysis, derived from WRF and CTSM output files.

Table B3. Variable Definition.

Variable name	Long name	Unit	Related fields in wrfout_d01.*.nc	Related fields in ctsm_lilac.clm2.*.nc
LST	Land surface temperature	$^{\circ}\mathrm{C}$	TSK - 273.15	FIRE (Equation 2)
LW_{down}	Downward longwave radiation	W/m^2	$GLW \times EMISS$	FLDS
LW_{up}	Upward longwave radiation	W/m^2	EMISS, TSK (Equation B9)	FIRE
$Q_{\rm h}$	Sensible heat flux	$\mathrm{W/m^2}$	HFX	FSH
Q_{le}	Latent heat flux	$\mathrm{W/m^2}$	LH	EFLX_LH_TOT
RH2M	2m near-surface relative humidity	%	T2, Q2, PSFC (Equation B5, B6)	RH2M
RH	Relative humidity of atmospheric layers	%	T, P, PB, QVAPOR (Equation B2, B3, B4)	-
SW_{down}	Downward solar radiation	$\mathrm{W/m^2}$	SWDOWN	FSDS
SW_{up}	Upward solar radiation	W/m^2	SWDOWN \cdot ALBEDO	FSR
T2M	2m near-surface canopy air temperature	°C	T2 - 273.15	TSA - 273.15
TA	Air temperature of atmospheric layers	°C	T, P, PB (Equation B1)	=
W10M	10m wind speed	m/s	U10, V10 (Equation B8)	U10
WIND	Wind speed of atmospheric layers	m/s	U, V (Equation B7)	-

¹ In the GM_SLUCM simulation, WRF saves historical fields from the atmospheric and land components into one file (i.e., wrfout_d01.*). The complete list and descriptions of WRF history fields are available at https://github.com/wrf-model/Users_Guide/blob/main/output_variables.rst (last access: 26 November 2025).

² In the GM_CLMU simulation, CTSM saves historical fields separately in output named ctsm_lilac.clm2.*.nc along with the default wrfout_d01.*.nc files. The ctsm_lilac is the default case name, which can be set by users. The complete list and descriptions of CTSM history fields are available at https://github.com/ESCOMP/CTSM/tree/master/doc/source/users_guide/setting-up-and-running-a-case/history_fields_nofates.rst (last access: 26 November 2025).

Atmospheric air temperature (TA) of a certain atmospheric layer is calculated as (Equation B1):

767

768

769

772

773

774

775

778

779

780

781

782

783

784

785

786

787

791

792

793

$$TA_l = (T_l + 300) \cdot \left(\frac{P_l + PB_l}{10^5}\right)^{\frac{R_d}{c_p}},$$
 (B1)

where l denotes the atmospheric layer. T is perturbation potential temperature (unit: K). P is perturbation pressure (unit: Pa). PB is the base state pressure (unit: Pa). R_d is the gas constant for dry air (287.05 J/kg K). c_p is the specific heat at constant pressure (typically 1004 J/kg K).

The relative humidity (RH) of a certain atmospheric layer is calculated as (Equation B2):

$$RH_l = \frac{e_l}{es_l} \cdot 100, \tag{B2}$$

where e_l is the actual vapor pressure, and es_l is the saturation vapor pressure. e_l and es_l are calculated as:

$$e_l = \frac{\text{QVAPOR}_l \cdot (P_l + PB_l)}{\epsilon + (1 - \epsilon) \cdot \text{QVAPOR}_l} \cdot \frac{1}{100},$$
(B3)

$$e_{l} = \frac{\text{QVAPOR}_{l} \cdot (\text{P}_{l} + \text{PB}_{l})}{\epsilon + (1 - \epsilon) \cdot \text{QVAPOR}_{l}} \cdot \frac{1}{100},$$

$$es_{l} = 6.112 \cdot \exp\left(\frac{17.67 \cdot (\text{TA}_{l} - 273.15)}{\text{TA}_{l} - 29.65}\right),$$
(B3)

where QVAPOR is water vapor mixing ratio (unit: kg/kg), ϵ is 0.622. Similarly, 2m rel-776 ative humidity (RH2M) is calculated through e and es: 777

$$e = \frac{\text{Q2} \cdot \text{PSFC}}{\epsilon + \text{Q2}} \cdot \frac{1}{100},\tag{B5}$$

$$e = \frac{\text{Q2} \cdot \text{PSFC}}{\epsilon + \text{Q2}} \cdot \frac{1}{100},$$

$$es = 6.112 \cdot \exp\left(\frac{17.67 \cdot (\text{T2} - 273.15)}{\text{T2} - 29.65}\right),$$
(B5)

where e is 2m actual vapor pressure, Q2 is 2m specific humidity, PSFC is surface pressure, and T2 is 2m air temperature.

Wind speed of a certain atmospheric layer is calculated as (Equation B7):

$$WIND = \sqrt{U_l^2 + V_l^2}, (B7)$$

where U_l and V_l is zonal and meridonal wind component, respectively. Similarly, 10m wind speed is calculated as (Equation B8):

$$W10M = \sqrt{U10_l^2 + V10_l^2}.$$
 (B8)

As WRF-SLUCM does not provide upward longwave radiation (LW_{up}) directly, it can be calculated as (Equation B9):

$$LW_{\text{up}} = \text{EMISS} \cdot \sigma \cdot \text{LST}^4,$$
 (B9)

where EMISS is the effective emissivity, σ is the Stefan–Boltzmann constant (5.67 × 10⁻⁸ W/m² K⁴, LST is land surface (skin) temperature in Kelvin.

B4 Computational Performance

The GM_CLMU simulation showed an obvious slowdown compared to the GM_SLUCM simulation at ARCHER2, where one standard node has two AMD EPYC 7742 64-core processors with 256 GB or 512 GB of memory. Under a time step of 6 s, we manipulated the number of CPUs per task (cpu-per-task) as 1, 2, 4, and 6. The number of tasks per node (ntasks) is set to 6, the maximum workable ntasks for our domain. We compare computational performance through three indices: total execution time, speed-up

ratio, total computation time, and residual time. The total execution time refers to the period from job start to completion, including computation, Input/Output, etc. The speed-up ratio is the result of the total execution time with 1 CPU divided by the counterpart with multiple CPUs. The total computation time is the sum of the elapsed time for every model time step. The residual time is the difference between the execution and computation time.

This experiment ran for one day for the GM_SLUCM and GM_CLMU simulations. We repeated GM_CLMU simulations under three configurations, one using the full plant functional types (PFTs) and urban land-unit types, one using one dominant PFT and full urban types, and one using one dominant PFT and one dominant urban type to simplify the CTSM structure.

When the cpu-per-task increases from 2 to 4, the total computation time in GM_SLUCM saw a moderate decrease, and then (Figure B1(a)). This indicated that adding too many CPUs could reduce parallel efficiency for simulations. Compared to WRF-SLUCM, it is more expensive to run WRF-CLMU, where the total execution time in the GM_CLMU simulation is more than twice that of the GM_SLUCM simulation. GM_CLMU saw a notable drop in execution and computation time, along with cpu-per-task increasing (Figure B1(c)). Given that CTSM is computationally intensive, increasing parallel processors and simplifying the default mosaic representation can improve simulation efficiency.

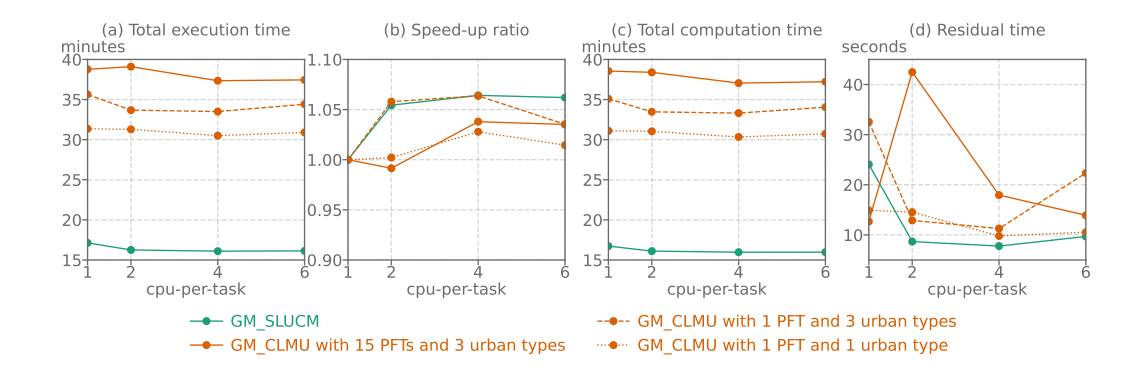


Figure B1. Timing of GM_SLUCM and GM_CLMU simulations. (a) Total execution time. (b) Speed-up ratio. (c) Total computation time. (d) Residual time, defined as the total execution time minus the total computation time.

Open Research Section

WRF source code is open access at https://github.com/wrf-model/WRF (last access: 26 November 2025). The CTSM-related implementation within WRF can be found in https://github.com/wrf-model/WRF/blob/master/phys/module_sf_ctsm.F, and the urban-related code is located in https://github.com/wrf-model/WRF/blob/master/phys/module_sf_urban.F (last access: 26 November 2025). Community Terrestrial Systems Model (CTSM) source code is available at: https://github.com/ESCOMP/CTSM, and Lightweight Infrastructure for Land-Atmosphere Coupling (LILAC) code is located in https://github.com/ESCOMP/CTSM/tree/master/src/cpl/lilac (last access: 26 November 2025) (CTSM Development Team, 2025). The Whitworth station dataset is accessed at (Centre for Aetmospheric Science - The University of Manchester, n.d.). The Hadley Centre Integrated Surface Database (HadISD) station dataset is accessed at (Met Office Hadley Centre & National Centers for Environmental Information - NOAA, 2025). The Manchester Air Quality Supersite (MAQS) dataset is accessed at (Watson, 2023b,

2023a). MODIS and VIIRS land surface temperature data refer to (Wan et al., 2021)
and (Hulley & Hook, 2023a, 2023b), respectively. They are accessed through the Google
Earth Engine platform: https://developers.google.com/earth-engine/datasets
(last access: 26 November 2025). The scripts and data to reproduce the results and figures are available at the authors' GitHub repository (Y. Sun & Zheng, 2025).

Acknowledgments

This work was supported by the Natural Environment Research Council [grant number UKRI1294]. This work used the ARCHER2 UK National Supercomputing Service (https://www.archer2.ac.uk) and JASMIN, the UK's collaborative data analysis environment (https://www.jasmin.ac.uk). Z.Z. appreciates the support provided by the academic start-up funds from the Department of Earth and Environmental Sciences at The University of Manchester. Y.S. is supported by Z.Z.'s academic start-up funds. The NSF National Center for Atmospheric Research is a major facility sponsored by the U.S. National Science Foundation under Cooperative Agreement No. 1852977.

References

- Barbano, F., Brattich, E., & Di Sabatino, S. (2021). Characteristic scales for turbulent exchange processes in a real urban canopy. *Boundary-Layer Meteorology*, 178(1), 119–142. doi: 10.1007/s10546-020-00554-5
- Buzan, J. R., Oleson, K. W., & Huber, M. (2015). Implementation and comparison of a suite of heat stress metrics within the Community Land Model version 4.5. Geoscientific Model Development, 8(2), 151–170. doi: 10.5194/gmd-8-151-2015
- Centre for Aetmospheric Science The University of Manchester. (n.d.). The Whitworth Observatory. Retrieved from https://www.cas.manchester.ac.uk/restools/whitworth/
- Chen, F., Kusaka, H., Bornstein, R., Ching, J., Grimmond, S., Grossman-Clarke, S., . . . Zhang, C. (2011). The integrated WRF/urban modelling system: Development, evaluation, and applications to urban environmental problems.

 International Journal of Climatology, 31(2), 273–288. doi: 10.1002/joc.2158
- Cheng, Y., Zhao, L., Chakraborty, T. C., Oleson, K., Demuzere, M., Liu, X., . . . Li, X. C. (2025). U-Surf: A global 1 km spatially continuous urban surface property dataset for kilometer-scale urban-resolving Earth system modeling. *Earth System Science Data*, 17(5), 2147–2174. doi: 10.5194/essd-17-2147-2025
- CTSM Development Team. (2024). ESCOMP/CTSM: Add LILAC (ctsm1.0.dev104) [Software]. Zenodo. doi: 10.5281/zenodo.11176758
- CTSM Development Team. (2025). ESCOMP/CTSM: CTSM 5.3: New surface datasets, git-fleximod intro, Leung dust, explicit AC, Matrix-CN, FATES transient LU, time/history metadata changes (ctsm5.3.021) [Software]. Zenodo. doi: 10.5281/zenodo.14768518
- CTSM-Norway. (2024). WRF-CTSM. Retrieved from https://metos-uio.github.io/CTSM-Norway-Documentation/wrf-ctsm/
- Danabasoglu, G., Lamarque, J.-F., Bacmeister, J., Bailey, D. A., DuVivier, A. K., Edwards, J., . . . Strand, W. G. (2020). The Community Earth System Model version 2 (CESM2). *Journal of Advances in Modeling Earth Systems*, 12(2), e2019MS001916. doi: 10.1029/2019MS001916
- Demuzere, M., He, C., Martilli, A., & Zonato, A. (2023). Technical documentation for the hybrid 100-m global land cover dataset with Local Climate Zones for WRF (1.0.0) [Dataset]. Zenodo. doi: 10.5281/zenodo.7670792
- Demuzere, M., Kittner, J., Martilli, A., Mills, G., Moede, C., Stewart, I. D., ...

 Bechtel, B. (2022). A global map of local climate zones to support earth system modelling and urban-scale environmental science. *Earth System Science*

Data, 14(8), 3835–3873. doi: 10.5194/essd-14-3835-2022

ຂຂດ

- Demuzere, M., Oleson, K. W., Coutts, A. M., Pigeon, G., & van Lipzig, N. P. M. (2013). Simulating the surface energy balance over two contrasting urban environments using the Community Land Model Urban. *International Journal of Climatology*, 33(15), 3182–3205. doi: 10.1002/joc.3656
- Duan, J., Zhou, J., Ma, J., Hou, Y., Wu, H., & Wang, Y. (2025). Hourly all-weather land surface temperature estimation through data assimilation of Fengyun-4A satellite observations and model simulations. *IEEE Transactions on Geoscience and Remote Sensing*, 63, 1–16. doi: 10.1109/TGRS.2025.3593942
- ESMF Core Team. (2025). esmf-org/ssmf: ESMF 8.9.0 (v8.9.0) [Software]. Zenodo. doi: 10.5281/zenodo.16884250
- Fairall, C. W., Bradley, E. F., Hare, J. E., Grachev, A. A., & Edson, J. B. (2003). Bulk parameterization of air–sea fluxes: Updates and verification for the COARE algorithm. *Journal of Climate*, 16(4), 571–591. doi: $10.1175/1520-0442(2003)016\langle0571:BPOASF\rangle2.0.CO;2$
- Gao, J., & O'Neill, B. C. (2020). Mapping global urban land for the 21st century with data-driven simulations and Shared Socioeconomic Pathways. Nature Communications, 11(1), 2302. doi: 10.1038/s41467-020-15788-7
- Georgescu, M., Broadbent, A. M., & Krayenhoff, E. S. (2024). Quantifying the decrease in heat exposure through adaptation and mitigation in twenty-first-century US cities. *Nature Cities*, 1(1), 42–50. doi: 10.1038/s44284-023-00001-9
- Grimmond, C. S. B., Blackett, M., Best, M. J., Baik, J.-J., Belcher, S. E., Beringer, J., ... Zhang, N. (2011). Initial results from phase 2 of the International Urban Energy Balance Model Comparison. *International Journal of Climatology*, 31(2), 244–272. doi: 10.1002/joc.2227
- Grimmond, C. S. B., Blackett, M., Best, M. J., Barlow, J., Baik, J.-J., Belcher, S. E., ... Zhang, N. (2010). The International Urban Energy Balance Models Comparison Project: First results from phase 1. *Journal of Applied Meteorology and Climatology*, 49(6), 1268–1292. doi: 10.1175/2010JAMC2354.1
- He, X., Li, Y., Wang, X., Chen, L., Yu, B., Zhang, Y., & Miao, S. (2019). High-resolution dataset of urban canopy parameters for Beijing and its application to the integrated WRF/Urban modelling system. *Journal of Cleaner Production*, 208, 373–383. doi: 10.1016/j.jclepro.2018.10.086
- Hersbach, H., Bell, B., Berrisford, P., Biavati, G., Horányi, A., Muñoz Sabater, J.,
 ... Thépaut, J.-N. (2023). ERA5 hourly data on pressure levels from 1940 to present [Dataset]. Copernicus Climate Change Service (C3S) Climate Data Store (CDS). doi: 10.24381/cds.bd0915c6
- Hong, S.-Y., & Lim, J.-O. J. (2006). The WRF Single-Moment 6-Class Microphysics Scheme (WSM6). Journal of the Korean Meteorological Society, 42(2), 129–151.
- Hong, S.-Y., Noh, Y., & Dudhia, J. (2006). A new vertical diffusion package with an explicit treatment of entrainment processes. *Monthly Weather Review*, 134 (9), 2318–2341. doi: 10.1175/MWR3199.1
- Hu, L., Brunsell, N. A., Monaghan, A. J., Barlage, M., & Wilhelmi, O. V. (2014). How can we use MODIS land surface temperature to validate long-term urban model simulations? *Journal of Geophysical Research: Atmospheres*, 119(6), 3185–3201. doi: 10.1002/2013JD021101
- Huang, H., Qian, Y., Bisht, G., Wang, J., Chakraborty, T., Hao, D., . . . Hetland, R. (2025). WRF-ELM v1.0: A regional climate model to study land–atmosphere interactions over heterogeneous land use regions. Geoscientific Model Development, 18(5), 1427–1443. doi: 10.5194/gmd-18-1427-2025
- Hulley, G., & Hook, S. (2023a). VIIRS/NPP land surface temperature/emissivity daily L3 global 1km SIN grid day V002 (002) [Dataset]. NASA Land Processes Distributed Active Archive Center. doi: 10.5067/VIIRS/VNP21A1D.002

Hulley, G., & Hook, S. (2023b). VIIRS/NPP land surface temperature/emissivity daily L3 global 1km SIN grid night V002 (002) [Dataset]. NASA Land Processes Distributed Active Archive Center. doi: 10.5067/VIIRS/VNP21A1N .002

- Iacono, M. J., Delamere, J. S., Mlawer, E. J., Shephard, M. W., Clough, S. A., & Collins, W. D. (2008). Radiative forcing by long-lived greenhouse gases: Calculations with the AER radiative transfer models. *Journal of Geophysical Research: Atmospheres*, 113(D13). doi: 10.1029/2008JD009944
- Imran, H. M., Kala, J., Ng, A. W. M., & Muthukumaran, S. (2018). An evaluation of the performance of a WRF multi-physics ensemble for heatwave events over the city of Melbourne in southeast Australia. *Climate Dynamics*, 50(7), 2553–2586. doi: 10.1007/s00382-017-3758-y
- Jackson, T. L., Feddema, J. J., Oleson, K. W., Bonan, G. B., & Bauer, J. T. (2010). Parameterization of urban characteristics for global climate modelling. *Annals of the Association of American Geographers*, 100(4), 848–865. doi: 10.1080/00045608.2010.497328
- Jerez, S., López-Romero, J. M., Turco, M., Lorente-Plazas, R., Gómez-Navarro, J. J., Jiménez-Guerrero, P., & Montávez, J. P. (2020). On the spin-up period in WRF simulations over Europe: Trade-offs between length and seasonality. *Journal of Advances in Modeling Earth Systems*, 12(4), e2019MS001945. doi: 10.1029/2019MS001945
- Joshi, P., Lin, T.-S., He, C., & Lamer, K. (2025). Urban weather modeling using WRF: Linking physical assumptions, code implementation, and observational needs. *Geoscientific Model Development*, 18(20), 7869–7890. doi: 10.5194/gmd-18-7869-2025
- Kadaverugu, R., Purohit, V., Matli, C., & Biniwale, R. (2021). Improving accuracy in simulation of urban wind flows by dynamic downscaling WRF with OpenFOAM. *Urban Climate*, 38, 100912. doi: 10.1016/j.uclim.2021.100912
- Kanda, M., Kanega, M., Kawai, T., Moriwaki, R., & Sugawara, H. (2007). Roughness lengths for momentum and heat derived from outdoor urban scale models. *Journal of Applied Meteorology and Climatology*, 46(7), 1067–1079. doi: 10.1175/JAM2500.1
- Karlický, J., Huszár, P., Halenka, T., Belda, M., Žák, M., Pišoft, P., & Mikšovský, J. (2018). Multi-model comparison of urban heat island modelling approaches. Atmospheric Chemistry and Physics, 18(14), 10655–10674. doi: 10.5194/acp-18-10655-2018
- Khan, A., Anand, P., Garshasbi, S., Khatun, R., Khorat, S., Hamdi, R., ... Santamouris, M. (2024). Rooftop photovoltaic solar panels warm up and cool down cities. *Nature Cities*, 1(11), 780–790. doi: 10.1038/s44284-024-00137-2
- Krayenhoff, E. S., Moustaoui, M., Broadbent, A. M., Gupta, V., & Georgescu, M. (2018). Diurnal interaction between urban expansion, climate change and adaptation in US cities. *Nature Climate Change*, 8(12), 1097–1103. doi: 10.1038/s41558-018-0320-9
- Kusaka, H., & Kimura, F. (2004). Coupling a single-layer urban canopy model with a simple atmospheric model: Impact on urban heat island simulation for an idealized case. *Journal of the Meteorological Society of Japan. Ser. II*, 82(1), 67–80. doi: 10.2151/jmsj.82.67
- Kusaka, H., Kondo, H., Kikegawa, Y., & Kimura, F. (2001). A simple single-layer urban canopy model for atmospheric models: Comparison with multi-layer and slab models. *Boundary-Layer Meteorology*, 101(3), 329–358. doi: 10.1023/A:1019207923078
- Lawrence, D. M., Fisher, R. A., Koven, C. D., Oleson, K. W., Swenson, S. C., Bonan, G., . . . Zeng, X. (2019). The Community Land Model version 5: Description of new features, benchmarking, and impact of forcing uncertainty.

 Journal of Advances in Modeling Earth Systems, 11(12), 4245–4287. doi:

10.1029/2018MS001583

aan

- Lee, S.-H., Lee, H., Park, S.-B., Woo, J.-W., Lee, D.-I., & Baik, J.-J. (2016). Impacts of in-canyon vegetation and canyon aspect ratio on the thermal environment of street canyons: Numerical investigation using a coupled WRF-VUCM model. Quarterly Journal of the Royal Meteorological Society, 142 (699), 2562–2578. doi: 10.1002/qj.2847
- Li, C., Zhang, N., Wang, Y., & Chen, Y. (2023). Modeling urban heat islands and thermal comfort during a heat wave event in East China with CLM5 incorporating local climate zones. *Journal of Geophysical Research: Atmospheres*, 128(16), e2023JD038883. doi: 10.1029/2023JD038883
- Li, D., Bou-Zeid, E., Barlage, M., Chen, F., & Smith, J. A. (2013). Development and evaluation of a mosaic approach in the WRF-Noah framework. *Journal of Geophysical Research: Atmospheres*, 118(21), 11,918–11,935. doi: 10.1002/2013JD020657
- Li, L., Bisht, G., Hao, D., & Leung, L. R. (2024). Global 1km land surface parameters for kilometer-scale Earth system modeling. *Earth System Science Data*, 16(4), 2007–2032. doi: 10.5194/essd-16-2007-2024
- Li, X. C., Zhao, L., Oleson, K., Zhou, Y., Qin, Y., Zhang, K., & Fang, B. (2024). Enhancing urban climate-energy modeling in the Community Earth System Model (CESM) through explicit representation of urban air-conditioning adoption. Journal of Advances in Modeling Earth Systems, 16(4), e2023MS004107. doi: 10.1029/2023MS004107
- Li, Z., Zhou, Y., Wan, B., Chung, H., Huang, B., & Liu, B. (2019). Model evaluation of high-resolution urban climate simulations: Using the WRF/Noah LSM/SLUCM model (Version 3.7.1) as a case study. Geoscientific Model Development, 12(11), 4571–4584. doi: 10.5194/gmd-12-4571-2019
- Liao, W., Li, Y., Liu, X., Wang, Y., Che, Y., Shao, L., . . . Chen, F. (2025). GloUCP: A global 1 km spatially continuous urban canopy parameters for the WRF model. *Earth System Science Data*, 17(6), 2535–2551. doi: 10.5194/essd-17-2535-2025
- Lipson, M. J., Grimmond, S., Best, M., Abramowitz, G., Coutts, A., Tapper, N., ... Pitman, A. J. (2023). Evaluation of 30 urban land surface models in the Urban-PLUMBER project: Phase 1 results. Quarterly Journal of the Royal Meteorological Society, 150(758), 126–169. doi: 10.1002/qj.4589
- Lipson, M. J., Grimmond, S., Best, M., Chow, W. T. L., Christen, A., Chrysoulakis, N., . . . Ward, H. C. (2022). Harmonized gap-filled datasets from 20 urban flux tower sites. *Earth System Science Data*, 14(11), 5157–5178. doi: 10.5194/essd-14-5157-2022
- Lipson, M. J., Grimmond, S., Best, M., Christen, A., Coutts, A., Crawford, B., . . . Kim, Y.-H. (2021). Urban-PLUMBER: Site information webpage (archive of https://urban-plumber.github.io/sites) (2021-09-20) [Dataset]. Zenodo. doi: 10.5281/zenodo.5516693
- Lombardozzi, D. L., Wieder, W. R., Sobhani, N., Bonan, G. B., Durden, D., Lenz, D., ... Pascucci, V. (2023). Overcoming barriers to enable convergence research by integrating ecological and climate sciences: The NCAR–NEON system Version 1. Geoscientific Model Development, 16(20), 5979–6000. doi: 10.5194/gmd-16-5979-2023
- Martilli, A., Clappier, A., & Rotach, M. W. (2002). An urban surface exchange parameterisation for mesoscale models. *Boundary-Layer Meteorology*, 104(2), 261–304. doi: 10.1023/A:1016099921195
- Masson, V. (2000). A physically-based scheme for the urban energy budget in atmospheric models. *Boundary-Layer Meteorology*, 94(3), 357–397. doi: 10.1023/A: 1002463829265
- Masson, V., Gomes, L., Pigeon, G., Liousse, C., Pont, V., Lagouarde, J.-P., ...

 Tulet, P. (2008). The Canopy and Aerosol Particles Interactions in TOulouse

Urban Layer (CAPITOUL) experiment. *Meteorology and Atmospheric Physics*, 102(3), 135–157. doi: 10.1007/s00703-008-0289-4

1047

1048

1049

1050

1051

1054

1055

1056

1057

1060

1061

1062

1063

1065

1066

1067

1068

1069

1071

1072

1073

1074

1075

1078

1079

1080

1081

1083

1084

1085

1086

1087

1090

1091

1092

1093

1094

1096

- Met Office Hadley Centre, & National Centers for Environmental Information NOAA. (2025). HadISD: Global sub-daily, surface meteorological station data, 1931-2024 (v3.4.1.2024f) [Dataset]. NERC EDS Centre for Environmental Data Analysis. doi: 10.5285/2a01faf75de64308b2bf4c7b43d393ef
 - Meyer, D., Schoetter, R., Riechert, M., Verrelle, A., Tewari, M., Dudhia, J., ...
 Grimmond, S. (2020). WRF-TEB: Implementation and evaluation of the coupled Weather Research and Forecasting (WRF) and Town Energy Balance (TEB) model. Journal of Advances in Modeling Earth Systems, 12(8), e2019MS001961. doi: 10.1029/2019MS001961
 - Monin, A. S., & Yaglom, A. M. (2013). Statistical fluid mechanics, volume ii: Mechanics of turbulence. Dover Publications.
 - Mužić, I., Hodnebrog, Ø., Yilmaz, Y. A., Berntsen, T. K., Lawrence, D. M., & Sobhani, N. (2025). The evaluation of hydroclimatic variables over Nordic Fennoscandia using WRF-CTSM. Journal of Geophysical Research: Atmospheres, 130(9), e2024JD043103. doi: 10.1029/2024JD043103
 - Oke, T. R., Mills, G., Christen, A., & Voogt, J. A. (2017). *Urban Climates*. Cambridge University Press.
 - Oleson, K. W., Bonan, G. B., Feddema, J. J., Vertenstein, M., & Kluzek, E. (2010). Technical description of an urban parameterization for the Community Land Model (CLMU) (Tech. Rep.). Boulder, Colorado: University Corporation for Atmospheric Research.
 - Oleson, K. W., & Feddema, J. (2020). Parameterization and surface data improvements and new capabilities for the Community Land Model Urban (CLMU). Journal of Advances in Modeling Earth Systems, 12(2), e2018MS001586. doi: 10.1029/2018MS001586
 - Oleson, K. W., Lawrence, D. M., Bonan, G. B., Drewniak, B., Huang, M., Levis, S., ... Yang, Z.-L. (2013). *Technical description of version 4.5 of the Community Land Model (CLM)* (Tech. Rep.). National Center for Atmospheric Research. doi: 10.5065/D6RR1W7M
 - Oleson, K. W., Lawrence, D. M., Bonan, G. B., Flanner, M., Kluzek, E., Lawrence, P., ... Zeng, X. (2010). *Technical description of version 4.0 of the Community Land Model (CLM)* (Tech. Rep.). Boulder, Colorado: National Center for Atmospheric Research.
 - Patel, P., Jamshidi, S., Nadimpalli, R., Aliaga, D. G., Mills, G., Chen, F., ...

 Niyogi, D. (2022). Modeling large-scale heatwave by incorporating enhanced urban representation. *Journal of Geophysical Research: Atmospheres*, 127(2), e2021JD035316. doi: 10.1029/2021JD035316
 - Qian, Y., Chakraborty, T. C., Li, J., Li, D., He, C., Sarangi, C., . . . Leung, L. R. (2022). Urbanization impact on regional climate and extreme weather: Current understanding, uncertainties, and future research directions. *Advances in Atmospheric Sciences*, 39, 819–860. doi: 10.1007/s00376-021-1371-9
 - Salamanca, F., & Martilli, A. (2010). A new building energy model coupled with an urban canopy parameterization for urban climate simulations—part II. Validation with one dimension off-line simulations. Theoretical and Applied Climatology, 99(3), 345–356. doi: 10.1007/s00704-009-0143-8
 - Salamanca, F., Zhang, Y., Barlage, M., Chen, F., Mahalov, A., & Miao, S. (2018). Evaluation of the WRF-Urban modeling system coupled to Noah and Noah-MP land surface models over a semiarid urban environment. *Journal of Geophysical Research: Atmospheres*, 123(5), 2387–2408. doi: 10.1002/2018JD028377
 - Schoetter, R., Kwok, Y. T., de Munck, C., Lau, K. K. L., Wong, W. K., & Masson, V. (2020). Multi-layer coupling between SURFEX-TEB-v9.0 and Meso-NH-v5.3 for modelling the urban climate of high-rise cities. *Geoscientific Model*

Development, 13(11), 5609–5643. doi: 10.5194/gmd-13-5609-2020

- Sharma, A., Fernando, H. J., Hamlet, A. F., Hellmann, J. J., Barlage, M., & Chen, F. (2017). Urban meteorological modeling using WRF: A sensitivity study. *International Journal of Climatology*, 37(4), 1885–1900. doi: 10.1002/joc.4819
- Skamarock, W. C., Klemp, J. B., Dudhia, J., Gill, D. O., Barker, D. M., Duda, M. G., ... Powers, J. G. (2019). A description of the Advanced Research WRF version 4 (Tech. Rep.). Boulder, Colorado, USA: National Center for Atmospheric Research.
- Sun, T., Omidvar, H., Li, Z., Zhang, N., Huang, W., Kotthaus, S., . . . Grimmond, S. (2024). WRF (v4.0)–SUEWS (v2018c) coupled system: Development, evaluation and application. *Geoscientific Model Development*, 17(1), 91–116. doi: 10.5194/gmd-17-91-2024
- Sun, Y., Fang, B., Oleson, K. W., Zhao, L., Topping, D. O., Schultz, D. M., & Zheng, Z. (2024). Improving urban climate adaptation modelling in the Community Earth System Model (CESM) through transient urban surface albedo representation. Journal of Advances in Modeling Earth Systems, 16, e2024MS004380. doi: 10.1029/2024MS004380
- Sun, Y., Oleson, K. W., Zhao, L., Mills, G., He, C., Demuzere, M., . . . Zheng, Z. (2025). Enhancing global-scale urban land cover representation using local climate zones in the Community Earth System Model. *Journal of Advances in Modeling Earth Systems*, 17(11), e2025MS004934. doi: 10.1029/2025MS004934
- Sun, Y., Oleson, K. W., & Zheng, Z. (2025). Modeling urban traffic heat flux in the Community Earth System Model. *EarthArXiv*. doi: 10.31223/X5ZX72
- Sun, Y., & Zheng, Z. (2025). envdes/code_WRF-CLMU: First release (v0.0.0) [Software]. Zenodo. doi: 10.5281/zenodo.17670407
- Takane, Y., Kikegawa, Y., Nakajima, K., & Kusaka, H. (2024). SLUCM+BEM (v1.0): A simple parameterisation for dynamic anthropogenic heat and electricity consumption in WRF-Urban (v4.3.2). Geoscientific Model Development, 17(23), 8639–8664. doi: 10.5194/gmd-17-8639-2024
- Tsiringakis, A., Steeneveld, G.-J., Holtslag, A. A. M., Kotthaus, S., & Grimmond, S. (2019). On- and off-line evaluation of the single-layer urban canopy model in London summertime conditions. *Quarterly Journal of the Royal Meteorological Society*, 145 (721), 1474–1489. doi: 10.1002/qj.3505
- Unger, J., Sümeghy, Z., & Zoboki, J. (2001). Temperature cross-section features in an urban area. Atmospheric Research, 58(2), 117-127. doi: 10.1016/S0169-8095(01)00087-4
- University Corporation for Atmospheric Research (UCAR). (2020). CTSM-LILAC user's guide (Tech. Rep.). University Corporation for Atmospheric Research (UCAR). Retrieved from https://escomp.github.io/CTSM/lilac/index.html
- Varquez, A. C. G., Kiyomoto, S., Khanh, D. N., & Kanda, M. (2021). Global 1-km present and future hourly anthropogenic heat flux. *Scientific Data*, 8(1), 64. doi: 10.1038/s41597-021-00850-w
- Wan, Z., Hook, S., & Hulley, G. (2021). MODIS/Aqua land surface temperature/emissivity daily L3 global 1km SIN grid V061 (061) [Dataset]. NASA Land Processes Distributed Active Archive Center. doi: 10.5067/MODIS/MYD11A1.061
- Wang, A., Barlage, M., Zeng, X., & Draper, C. S. (2014). Comparison of land skin temperature from a land model, remote sensing, and in situ measurement. *Journal of Geophysical Research: Atmospheres*, 119(6), 3093–3106. doi: 10.1002/2013JD021026
- Wang, C., Wang, Z.-H., & Ryu, Y.-H. (2021). A single-layer urban canopy model with transmissive radiation exchange between trees and street canyons. *Building and Environment*, 191, 107593. doi: 10.1016/j.buildenv.2021.107593

Wang, L., Huang, M., & Li, D. (2021). Strong influence of convective heat transfer efficiency on the cooling benefits of green roof irrigation. *Environmental Research Letters*, 16(8), 084062. doi: 10.1088/1748-9326/ac18ea

- Wang, L., Li, D., & Yuan, X. (2025). The role of vapor pressure deficit in the CLM simulated interaction between urban heat islands and heat waves over conus. Geophysical Research Letters, 52(6), e2024GL113257. doi: 10.1029/2024GL113257
- Watson, N. (2023a). Dataset record: Meteorological data from Palas FIDAS 200 instrument at Manchester Air Quality Site, 2019 onwards [Dataset]. NERC EDS Centre for Environmental Data Analysis. Retrieved from https://catalogue.ceda.ac.uk/uuid/62af3c6051044460aa0a716e2204bffc
- Watson, N. (2023b). Dataset record: Wind speed and direction data from Gill sonic windmaster instrument at the Manchester Air Quality Site, 2019 onwards [Dataset]. NERC EDS Centre for Environmental Data Analysis. Retrieved from https://catalogue.ceda.ac.uk/uuid/91625bdf73944c5e896eb56d1fec35ee/
- Wilson, T. H., & Fovell, R. G. (2018). Modeling the evolution and life cycle of radiative cold pools and fog. Weather and Forecasting, 33(1), 203–220. doi: 10.1175/WAF-D-17-0109.1
- Xu, X., Li, X., Wang, X., He, C., Tian, W., Tian, J., & Yang, L. (2020). Estimating daily evapotranspiration in the agricultural-pastoral ecotone in Northwest China: A comparative analysis of the complementary relationship, WRF-CLM4.0, and WRF-Noah methods. Science of The Total Environment, 729, 138635. doi: 10.1016/j.scitotenv.2020.138635
- Yang, J., Wang, Z.-H., Chen, F., Miao, S., Tewari, M., Voogt, J. A., & Myint, S. (2015). Enhancing hydrologic modelling in the coupled weather research and forecasting—urban modelling system. *Boundary-Layer Meteorology*, 155(1), 87–109. doi: 10.1007/s10546-014-9991-6
- Yu, J., Sun, Y., Lindley, S., Jay, C., Topping, D. O., Oleson, K. W., & Zheng, Z. (2025). Integration and execution of Community Land Model Urban (CLMU) in a containerized environment. *Environmental Modelling & Software*, 188, 106391. doi: 10.1016/j.envsoft.2025.106391
- Zhang, K., Fang, B., Oleson, K., Zhao, L., He, C., Huang, Q., . . . Lee, X. (2025). Urban land expansion amplifies surface warming more in dry climate than in wet climate: A global sensitivity study. *Journal of Geophysical Research:* Atmospheres, 130(4), e2024JD041696. doi: 10.1029/2024JD041696
- Zhang, K., Wang, R., Shen, C., & Da, L. (2010). Temporal and spatial characteristics of the urban heat island during rapid urbanization in Shanghai, China. *Environmental Monitoring and Assessment*, 169(1), 101–112. doi: 10.1007/s10661-009-1154-8
- Zhang, X., Chen, W., Chen, Z., Yang, F., Meng, C., Gou, P., ... Wang, Z. (2022). Construction of cloud-free MODIS-like land surface temperatures coupled with a regional weather research and forecasting (WRF) model. *Atmospheric Environment*, 283, 119190. doi: 10.1016/j.atmosenv.2022.119190
- Zhao, L., Oleson, K. W., Bou-Zeid, E., Krayenhoff, E. S., Bray, A., Zhu, Q., ... Oppenheimer, M. (2021). Global multi-model projections of local urban climates. *Nature Climate Change*, 11(2), 152–157. doi: 10.1038/s41558-020-00958-8
- Zheng, Z., Zhao, L., & Oleson, K. W. (2021). Large model structural uncertainty in global projections of urban heat waves. *Nature Communications*, 12(1), 3736. doi: 10.1038/s41467-021-24113-9